

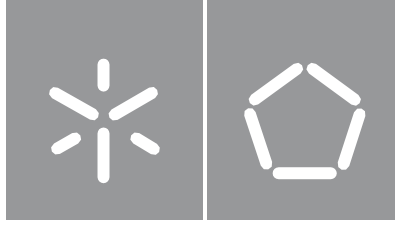


Mariana Santos Amorim

**Development of a biosensor based on
plastic antibodies for the isolation
and detection of extracellular vesicles**

Universidade do Minho
Escola de Engenharia





Universidade do Minho
Escola de Engenharia

Mariana Santos Amorim

**Development of a biosensor based on
plastic antibodies for the isolation and
detection of extracellular vesicles**

Dissertação de Mestrado
Mestrado Integrado em Engenharia Biológica

Trabalho efetuado sob a orientação da
**Professora Doutora Maria Madalena dos
Santos Alves**
e da
**Doutora Manuela Maria Teixeira Basto de
Faria Frasco**

Direitos de autor e condições de utilização do trabalho por terceiros

Este é um trabalho académico que pode ser utilizado por terceiros desde que respeitadas as regras e boas práticas internacionalmente aceites, no que concerne aos direitos de autor e direitos conexos.

Assim, o presente trabalho pode ser utilizado nos termos previstos na licença abaixo indicada.

Caso o utilizador necessite de permissão para poder fazer um uso do trabalho em condições não previstas no licenciamento indicado, deverá contactar o autor, através do RepositóriUM da Universidade do Minho.

Licença concedida aos utilizadores deste trabalho



Atribuição-NãoComercial-SemDerivações

CC BY-NC-ND

<https://creativecommons.org/licenses/by-nc-nd/4.0/>

Acknowledgments

To all those who contributed to the realization of this work, directly or indirectly, I would like to express my sincere gratitude.

To Professor Madalena Alves for having introduced me to this project, giving me the opportunity to participate in it, for her constant help and availability.

To Dr.^a Manuela Frasco, whose patience, companionship, teaching, support and constant presence were absolutely essential for the elaboration of this work.

To Professor Goreti Sales for the opportunity to join this project, for her guidance, support and trust.

To the BioMark@UC group and all its members for my integration into the team, constant support, for making available the facilities and any equipment that might be necessary to carry out the work.

To all colleagues, professors and employees of the Department of Chemical Engineering of the University of Coimbra who, in one way or another, offered the necessary conditions to carry out this work.

To all the professors at the University of Minho who were part of my academic path and to whom I just have to express my sincere thanks for all the teachings they provided.

To my classmates and friends who made this journey unique and unforgettable.

To my parents, my brother, my boyfriend and my entire family for all the effort they made so that I was able to successfully complete this chapter of my life, giving me their constant and unconditional care and support. To them I will be eternally grateful.

Finally, I would also like to thank the European Commission for funding through the MindGAP project (FET-Open/H2020/GA829040).

To all,

A sincere thank you.

Statement of integrity

I hereby declare having conducted this academic work with integrity. I confirm that I have not used plagiarism or any form of undue use of information or falsification of results along the process leading to its elaboration.

I further declare that I have fully acknowledged the Code of Ethical Conduct of the University of Minho.

Desenvolvimento de um biossensor baseado em anticorpos plásticos para isolamento e detecção de vesículas extracelulares

Resumo

As vesículas extracelulares são nanovesículas libertadas pelas células que participam na comunicação intercelular, afetando os processos fisiológicos e patológicos. Estas vesículas transportam inúmeras biomoléculas, incluindo ácidos nucleicos, proteínas e lípidos e, por isso, têm sido amplamente estudadas como novos biomarcadores em biópsias líquidas, podendo a sua identificação ser utilizada para deteção precoce de doenças através de diagnósticos minimamente invasivos e terapias de última geração. No entanto, a heterogeneidade das vesículas extracelulares e a complexidade dos fluidos biológicos requerem o desenvolvimento de métodos mais eficientes para o seu isolamento e deteção. Nesse sentido, o principal objetivo deste trabalho é apresentar uma nova tecnologia baseada em polímeros molecularmente impressos para o isolamento destas vesículas. Estes materiais poliméricos sintéticos são estáveis, fáceis de produzir, e contêm locais de reconhecimento específicos para o composto alvo, permitindo a sua ligação seletiva e subsequente deteção com alta sensibilidade.

Neste trabalho, foi desenvolvido um novo polímero fotónico impresso molecularmente como sensor para isolamento e deteção de vesículas extracelulares. O sensor proposto tem por base a fabricação de uma estrutura fotónica formada por esferas coloidais integrada num hidrogel impresso. A proteína CD9 presente na superfície das vesículas foi utilizada como molécula de impressão e as propriedades analíticas do sensor com base no sinal ótico foram inicialmente analisadas quanto ao reconhecimento da CD9. O sensor apresentou uma resposta linear entre 25 pg mL^{-1} e 2344 pg mL^{-1} de CD9 e um limite de deteção de 19 pg mL^{-1} de CD9 em soro humano, para além de ter demonstrado seletividade para a CD9 em comparação com outros biomarcadores proteicos existentes nas vesículas extracelulares. Além disso, o sensor foi capaz de detetar vesículas extracelulares em soro humano, na gama de $6,85 \times 10^1 \text{ } \mu\text{L}^{-1}$ – $6,85 \times 10^5 \text{ } \mu\text{L}^{-1}$. O material sensor desenvolvido é bastante promissor, para a deteção e o isolamento de vesículas extracelulares, oferecendo vantagens do ponto de vista de custo e sensibilidade, relativamente às técnicas de isolamento convencionais.

Palavras-chave: Cristais fotónicos; Diagnóstico de doenças; Polímeros de impressão molecular; Proteína CD9; Vesículas extracelulares.

Development of a biosensor based on plastic antibodies for the isolation and detection of extracellular vesicles

Abstract

Extracellular vesicles are nanoscale vesicles released by cells that participate in intercellular communication, and thus affect physiological and pathological processes. Due to their biomolecular cargo, composed of nucleic acids, proteins, and lipids, extensive studies have been pursued on extracellular vesicles as novel biomarkers in liquid biopsies. Therefore, the ability to identify them is a powerful tool for early detection of diseases through minimally invasive diagnostics and next-generation therapies. However, due to the heterogeneity of extracellular vesicles and the complexity of biofluids, more efficient methods for their isolation and detection need to be developed. In this regard, the main objective of this thesis is to introduce a novel technology for the isolation of extracellular vesicles based on molecularly imprinted polymers. These synthetic polymeric materials are stable, easy to produce, and contain specific recognition sites for the target compound, allowing their selective binding and detection with high sensitivity.

Herein, a novel molecularly imprinted photonic polymer sensor was developed for isolation and detection of extracellular vesicles. The sensor design is based on the fabrication of an imprinted hydrogel integrating a photonic structure formed by the self-assembly of colloidal spheres. The CD9 protein present on the surface of the vesicles was used as imprinting molecule and the analytical properties of the sensor based on the optical signal were first assayed for CD9 recognition. The sensor displayed a linear response from 25 pg mL^{-1} to 2344 pg mL^{-1} of CD9 and a limit of detection of 19 pg mL^{-1} of CD9 in human serum, demonstrating also to be selective for CD9 when compared to other protein biomarkers present in extracellular vesicles. In addition, the sensor detected extracellular vesicles in the range of $6.85 \times 10^1 \text{ } \mu\text{L}^{-1}$ – $6.85 \times 10^5 \text{ } \mu\text{L}^{-1}$ in human serum. Overall, the developed sensing material based on molecular imprinting technology is a promising cost-effective and simple alternative to conventional isolation procedures as a sensitive method for the detection and isolation of extracellular vesicles.

Keywords: CD9 protein; Diagnosis of diseases; Extracellular vesicles; Molecularly imprinted polymers; Photonic crystals.

Table of contents

Direitos de autor e condições de utilização do trabalho por terceiros	i
Acknowledgments	ii
Statement of integrity	iii
Resumo	iv
Abstract	v
List of nomenclature.....	viii
List of symbols.....	ix
List of figures	x
List of tables.....	xii
Chapter 1. Introduction	1
1.1. Outline of the thesis.....	1
1.2. State-of-the-art.....	1
1.2.1. Extracellular vesicles	1
1.2.1.1. Biogenesis and composition.....	2
1.2.1.2. Biological purposes and applications.....	4
1.2.1.3. Separation and concentration methods.....	6
1.2.1.3.1. Density-based isolation	6
1.2.1.3.2. Size-based isolation.....	7
1.2.1.3.3. Immunoaffinity-based isolation.....	7
1.2.1.4. Characterization.....	7
1.2.2. Biosensors.....	8
1.2.2.1. Biorecognition using MIPs.....	8
1.2.2.1.1. MIP synthesis.....	8
1.2.2.1.2. Application of MIPs for the recognition of EVs.....	11
1.2.2.2. Optical detection based on photonic crystals	11

1.2.2.3. Molecularly imprinted photonic polymers.....	18
1.3. Objectives of the thesis	19
Chapter 2. Materials and methods	20
2.1. Reagents	21
2.2. Synthesis of PMMA colloidal spheres.....	21
2.3. Opal construction	22
2.4. Hydrogel-based MIPP for recognition of CD9 protein.....	23
2.5. Characterization of the sensing materials	24
2.6. Sensing ability of the hydrogel-based MIPP towards the CD9 protein.....	24
2.7. Recognition ability of the hydrogel-based MIPP towards EVs.....	26
2.8. Selectivity studies by testing CD81 and GLAST-1 proteins	26
Chapter 3. Results and discussion.....	27
3.1. Characterization of the PMMA colloidal spheres	27
3.1.1. ATR-FTIR analysis.....	27
3.1.2. SEM and DLS analysis	28
3.2. Characterization of the PMMA opal film.....	29
3.3. Characterization of the hydrogel-based MIPP	31
3.4. Optical response of the hydrogel-based MIPP towards the CD9 protein	32
3.5. Optical response of the hydrogel-based MIPP towards EVs.....	35
3.6. Selectivity studies by testing CD81 and GLAST-1 proteins	36
Chapter 4. Conclusions and future work	38
Bibliography	39

List of nomenclature

Abbreviations

1D - One-dimensional

2D - Two-dimensional

3D - Three-dimensional

AAm - Acrylamide

ANOVA - Analysis of variance

ATR-FTIR - Attenuated total reflectance-Fourier transform infrared spectroscopy

Bis-A - *N,N'*-methylenebisacrylamide

DLS - Dynamic light scattering

ELISA - Enzyme-linked immunosorbent assay

EVs - Extracellular vesicles

fcc - Face-centered cubic

HEMA - 2-hydroxyethyl methacrylate

ISEV - International society for extracellular vesicles

KPS - Potassium persulfate

MIPPs - Molecularly imprinted photonic polymers

MIPs - Molecularly imprinted polymers

MMA - Methyl methacrylate

MVBs - Multivesicular bodies

NIPP - Non-molecularly imprinted photonic polymer

PBG - Photonic band gap

PBS - Phosphate-buffered saline

PDI - Polydispersity index

PhCs - Photonic crystals

PMMA - Poly(methyl methacrylate)

PS - Polystyrene

SEM - Scanning electron microscope

TEMED - *N,N,N',N'*-tetramethylethylenediamine

List of symbols

$\%_{\text{error}}$ - Percent error

D_{avg} - Average diameter

exp_{value} - Expected value

m_{value} - Measured value

n_{eff} - Effective refractive index

I - Maximum reflectance intensity

I/I_0 - Relative reflectance intensity

I_0 - Maximum reflectance intensity of the control

LOD - Limit of detection

d - Diffracting plane spacing

m - Order of the Bragg diffraction

θ - Angle of light incidence

κ - Conductivity

λ - Wavelength of the reflected light

ν - Wavenumber

List of figures

FIGURE 1-1 FRAMEWORK OF THE THESIS.....	1
FIGURE 1-2 SCHEMATIC REPRESENTATION OF THE DIFFERENT TYPES OF MEMBRANE VESICLES RELEASED BY CELLS, EITHER BY DIRECT OUTWARD BUDDING OF THE PLASMA MEMBRANE OR BY FUSION OF INTERNAL MVBS WITH THE PLASMA MEMBRANE ³	3
FIGURE 1-3 SCHEMATIC REPRESENTATION OF CELL-TO-CELL COMMUNICATION THROUGH EVs: EVs DERIVED FROM CELLS TRANSFER NUCLEIC ACIDS AND PROTEINS TO THE SURROUNDING, AS WELL AS TO DISTANT CELLS.	5
FIGURE 1-4 SCHEME OF THE MOLECULAR IMPRINTING PROCESS.	9
FIGURE 1-5 APPROACHES FOR THE SYNTHESIS OF MIPs.....	10
FIGURE 1-6 PHOTONIC SENSORS ARE DEVELOPED AS 1D, 2D OR 3D STRUCTURES IN SEVERAL CONFIGURATIONS.	14
FIGURE 2-1 SENSOR CONSTRUCTION INVOLVES THE SYNTHESIS OF MONODISPERSE PMMA COLLOIDAL SPHERES AND THEIR SELF-ASSEMBLY ON GLASS SUBSTRATES, PREPARATION OF HYDROGEL-BASED MIPP FOR CD9 PROTEIN AND STUDY THE ANALYTICAL RESPONSE OF THE MIPP SENSOR TOWARDS CD9 PROTEIN AND THE RECOGNITION ABILITY OF EVs.	20
FIGURE 2-2 SCHEMATIC ILLUSTRATION OF THE VERTICAL DEPOSITION PROCESS. PMMA COLLOIDAL SPHERES SELF-ASSEMBLE BY SOLVENT EVAPORATION AND FORM A PHC FILM.	22
FIGURE 2-3 SCHEMATIC REPRESENTATION OF THE FORMATION OF BRIDGES BETWEEN ADJACENT PMMA SPHERES. ...	23
FIGURE 3-1 ATR-FTIR SPECTRUM OF THE SYNTHESIZED PMMA COLLOIDAL SPHERES.....	27
FIGURE 3-2 SEM MICROGRAPHS OF THE PMMA COLLOIDAL SPHERES: (A) 50000× AND (B) 100000×. THE INSET PRESENTS THE SIZE DISTRIBUTION HISTOGRAM OF THE PMMA SPHERES OF THE SAMPLE.	28
FIGURE 3-3 SEM IMAGES OF PMMA OPALS, SHOWING SELF-ASSEMBLED SPHERES: (A) CROSS-SECTIONAL 15000×, (B) TOP VIEW 10000× AND (C) TOP VIEW 30000× WITH AN INSET ILLUSTRATING THE CLOSE-PACKING FCC (BLACK HEXAGON IN THE IMAGE).....	30
FIGURE 3-4 REFLECTANCE SPECTRUM OF THE OPAL STRUCTURE (INCIDENT LIGHT AT AN ANGLE OF 45°).	31
FIGURE 3-5 SEM IMAGES OF THE HYDROGEL-BASED MIPP, SHOWING THE IMPRINTING OF THE PMMA OPAL STRUCTURE: (A) CROSS-SECTIONAL 40000× AND (B) TOP VIEW 50000× WITH WHITE HEXAGONS ILLUSTRATING THE CLOSE-PACKING THAT WAS KEPT IN THE HYDROGEL.	31
FIGURE 3-6 REFLECTANCE SPECTRUM OF THE HYDROGEL-BASED MIPP (INCIDENT LIGHT AT AN ANGLE OF 45°).	32
FIGURE 3-7 OPTICAL RESPONSE OF THE HYDROGEL-BASED MIPP (A, B) AND THE NIPP CONTROL (C, D) TO CD9 PROTEIN IN PBS BUFFER (0.01 MOL L ⁻¹ , PH = 7.4) (A, C) AND IN HUMAN SERUM (1000-FOLD DILUTED) (B, D), EXPRESSED	

BY REFLECTANCE INTENSITY, AND THE CORRESPONDING CALIBRATION CURVES IN PBS BUFFER (E) AND IN SERUM (F) (N=3).....	34
FIGURE 3-8 RESPONSE OF THE SENSOR MIPP AND RESPECTIVE NIPP CONTROL TO THREE DIFFERENT EVs UNITARY CONCENTRATIONS ($6.85 \times 10^1 \mu\text{L}^{-1}$, $6.85 \times 10^3 \mu\text{L}^{-1}$ AND $6.85 \times 10^5 \mu\text{L}^{-1}$) PREPARED IN HUMAN SERUM (DILUTED 1000-FOLD) (N=3).....	36
FIGURE 3-9 RESPONSE OF THE SENSOR MIPP AND RESPECTIVE NIPP CONTROL TO TWO DIFFERENT CD81 (A) AND GLAST-1 (B) PROTEIN CONCENTRATIONS (100 PG ML^{-1} AND 1000 PG ML^{-1}) PREPARED IN HUMAN SERUM (DILUTED 1000-FOLD) (N=3).....	37

List of tables

TABLE 1-1 EVS HAVE BEEN BROADLY CLASSIFIED INTO EXOSOMES, MICROVESICLES, AND APOPTOTIC BODIES ACCORDING TO THEIR CELLULAR ORIGIN, SIZE, FUNCTION AND CONTENTS ^{4,5,8}	2
TABLE 1-2 SEPARATION OF EVS BASED ON DENSITY: ULTRACENTRIFUGATION AND CENTRIFUGATION WITH PRECIPITATION REAGENTS ^{1,2}	6
TABLE 1-3 METHODS COMMONLY USED FOR COLLOIDAL ASSEMBLY ⁴⁰⁻⁵⁶	15
TABLE 1-4 EXAMPLES OF MIPPS: TARGET MOLECULE, SPHERES USED AS PHC TEMPLATE, SELF-ASSEMBLY METHOD, AND PHC'S FINAL DESIGN IN THE PHOTONIC SENSOR ⁵⁷⁻⁸¹	18

Chapter 1. Introduction

1.1. Outline of the thesis

This thesis has been subdivided into four chapters, as illustrated in Figure 1-1.

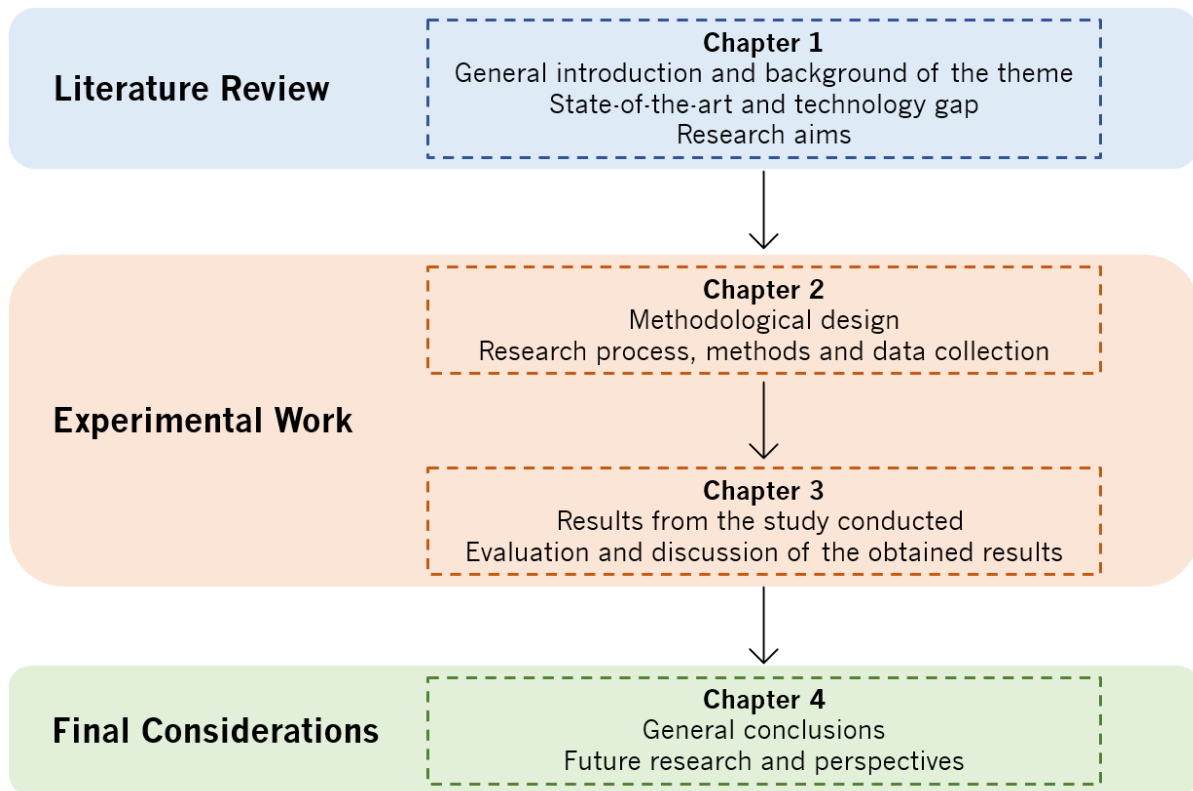


Figure 1-1 Framework of the thesis.

1.2. State-of-the-art

1.2.1. Extracellular vesicles

Extracellular vesicles (EVs) are membrane vesicles secreted by most cell types into the surrounding environment, mediating intercellular communication at both paracrine and systemic levels¹, and are present in body fluids (*e.g.*, blood, urine, amniotic fluid, saliva, ascites, cerebrospinal fluid)². When they were discovered, EVs were thought to be involved in cellular excretion of by-products², being merely viewed as a mean for cells to dispose of unwanted components³ and not much attention was given to them until their participation in the immune response was revealed. Only later on, in 2007, it was described that they mediate communication between cells due to the presence of functional RNAs². Since then, it has been a fruitful research field and is originating much understanding in cell-cell communication with applications in novel diagnostic and therapeutic approaches.

1.2.1.1. Biogenesis and composition

EVs are a complex group of vesicles constituted by three main subtypes: exosomes, microvesicles, and apoptotic bodies¹, which can be differentiated based upon their biogenesis, release pathways, size, content and function^{4,5} (Table 1-1). These vesicles are originated from distinct subcellular compartments and their proportions vary depending on the physiological state and cell type of origin¹. Also, the differential origin of EVs affects their specific cargos¹, that consist of lipids, nucleic acids and proteins⁵, which have an impact on the functionality of EVs and constitute a molecular fingerprint of the cell of origin¹.

Exosomes are vesicles smaller than approximately 150 nm in diameter⁴, originated in the endosomal system and are, thus, enriched in endosome-derived components⁶. The internal budding of the cytomembrane gives rise to early endosomes that mature to multivesicular bodies (MVBs). Intraluminal vesicles are formed inside the lumen of MVBs through inward budding of the endosomal membrane. These MVBs can either fuse with lysosome and be degraded or with the cell membrane, where their contents will be secreted out of the cell as exosomes⁷ (Figure 1-2). Despite the fact that there is still much to be understood regarding the exact mechanism of biogenesis and its regulation, it appears the formation of MVBs can be stimulated by growth factors and the cell adjusts its exosome production according to its needs, making exosomes picturing their cells of origin⁵.

Table 1-1 EVs have been broadly classified into exosomes, microvesicles, and apoptotic bodies according to their cellular origin, size, function and contents^{4,5,8}

	Exosomes	Microvesicles	Apoptotic Bodies
Origin	Endocytic pathway	Plasma membrane	Plasma membrane
Size	30 nm - 150 nm	50 nm - 1000 nm	100 nm - 5000 nm
Function	Intercellular communication	Intercellular communication	Phagocytic clearance of apoptotic cells
Contents	Proteins, nucleic acids (DNA, mRNA, miRNAs, and other non-coding RNAs), lipids	Proteins, nucleic acids (DNA, mRNA, miRNAs, and other non-coding RNAs), lipids	Cytosolic content, cell organelles

Microvesicles are EVs whose size typically ranges from 50 nm to 1000 nm, which are formed by direct outward budding of the cell's plasma membrane⁴ (Figure 1-2). Although the route of microvesicles formation is not entirely known, it is thought to require cytoskeleton components, molecular motors and fusion machinery, and it depends on the parent cell's physiological state and microenvironment⁵.

Lastly, apoptotic bodies have a broad size range and are released by dying cells into the extracellular space. The apoptotic bodies form by separation of the plasma membrane from the cytoskeleton, resulting from the increased hydrostatic pressure after the cell contracts^{4,5}.

These EVs have different cargo profiles due to their different routes of formation, despite a substantial overlap that is often observed. Thus, no consensus on marker classification has been established to differentiate the various subtypes of EVs⁹. In addition, the lack of standardized isolation and analysis methods of EVs, results in proteomic profiles from the same source to be dependent on their isolation method⁵. Considering these hurdles regarding the overlapping of EV markers that could give researchers confidence on the EV subtype in study, some degree of heterogeneity in the nomenclature, and the need to implement crucial requirements for standardization of the methods, the current guidelines from the International Society for Extracellular Vesicles¹⁰ (ISEV) recommend adopting the uniform terminology of EVs unless there is unequivocal determination of EV identity. Thus, herein, the use of EVs throughout the text is followed.

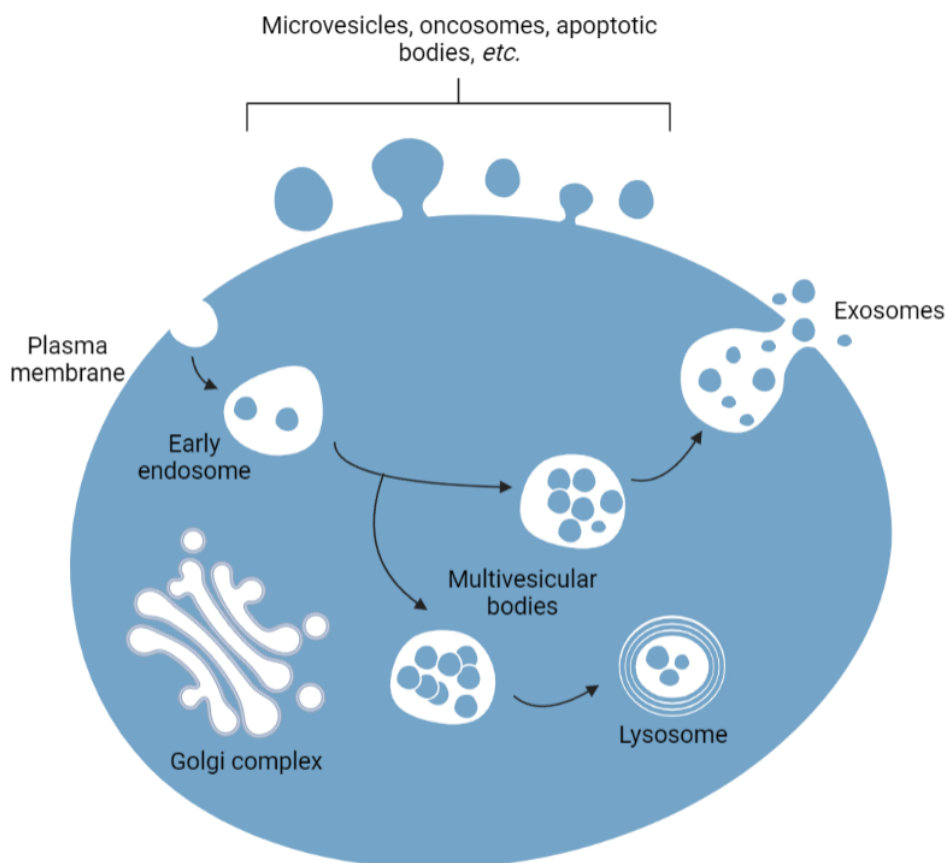


Figure 1-2 Schematic representation of the different types of membrane vesicles released by cells, either by direct outward budding of the plasma membrane or by fusion of internal MVBs with the plasma membrane³.

Numerous studies have identified that EVs facilitate cellular communication in many biological processes by delivering functional cargos such as proteins, mRNA, and miRNA. Indeed, EVs contain different compositions and perform different functions depending on the cell type and status. In general, EVs are composed by lipids (*e.g.*, sphingolipids, cholesterol), proteins (*e.g.*, tetraspanins, adhesion molecules) and genetic material (including DNA and non-coding RNAs). The components of EVs vary depending on the cell of origin, and thousands of different proteins, miRNAs, mRNAs and lipids have been identified in these vesicles^{7,11,12}.

Tetraspanins such as CD9, CD81 and CD63, are of particular interest because EVs are highly enriched in this protein family. They are involved in protein biogenesis, EVs production and vesicular cargo sorting, and thus, they significantly affect the function of vesicles. Furthermore, they can modulate the membrane curvature of the vesicles to enable EV budding and may be involved in EV fission from the parent cell membrane, and thus, directly participating in EV formation^{13,14}. Owing to this crucial role, tetraspanins are most often used as specific markers of EVs and for their isolation by immunoaffinity methods. Following the guidelines proposed by the ISEV, the analysis of tetraspanins as part of the protein content-based EV characterization is used for demonstrating the EV nature and the degree of purity of an EV preparation¹³.

1.2.1.2. Biological purposes and applications

Most biological functions attributed to EVs have been studied after their isolation from cell cultures or biological fluids. EVs participate in cell-cell communication, contributing to a myriad of functions like cell maintenance, tumour progression and stimulation of immune responses by acting as antigen-presenting vesicles. Thus, they are not only essential in the processes of normal physiology, such as immune response, cell proliferation, inflammation, lactation, and neuronal function but are also implicated in the different stages of disease progression such as hepatic, neurodegenerative, and cancer diseases. For example, in the nervous system, EVs may help promoting myelin formation, neurite growth and neuronal survival. While EVs have an important role in tissue repair and regeneration, it has been found at the same time that EVs contain pathogenic proteins (*e.g.*, beta-amyloid peptide, alpha-synuclein) that may contribute to neurodegenerative progression⁵. Thus, EVs are involved in both normal physiological processes and disease progression in a pleiotropic manner².

The transfer of EVs mainly follows two procedures: their secretion from the parental cells and fusion with the recipient cells. After being released from the parental cell, EVs carrying information from

this cell will fuse with recipient cells and release the information they contain, which further causes corresponding biological effects⁷ (Figure 1-3).

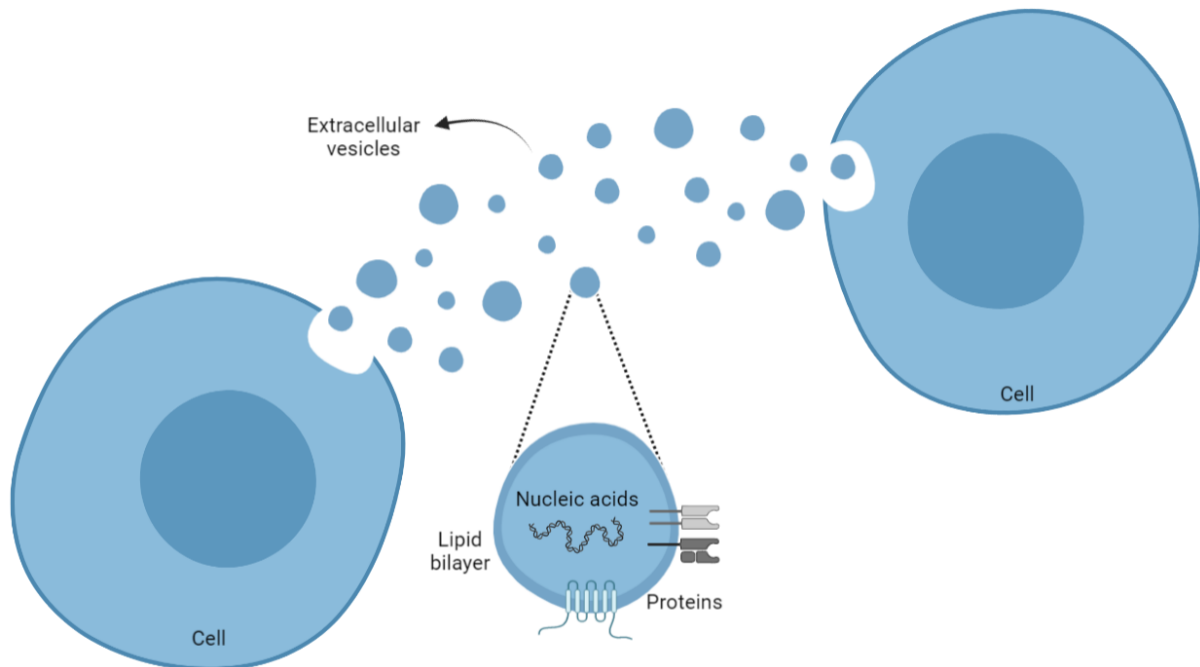


Figure 1-3 Schematic representation of cell-to-cell communication through EVs: EVs derived from cells transfer nucleic acids and proteins to the surrounding, as well as to distant cells.

The study of EVs as carriers of biomarkers is ideal because these vesicles are found in body fluids, which could allow minimally to non-invasive liquid biopsies for diagnostic and prognostic purposes. If the disease marker directly correlates to the disease state, and if the patient's treatment is working, a change in the presence of the biomarker should be observed as the patient undergoes treatment. For example, EVs in both plasma and cerebrospinal fluid have been found to contain alpha-synuclein, a protein associated with Parkinson's disease and EVs isolated from urine have demonstrated the ability to reflect acute kidney injury. There has also been a success in finding markers for pancreatic cancer and lung cancer in EVs as well⁵.

The understanding of cell-cell communication has been profiting from the advances reached in the field of EVs. Moreover, EVs represent a very important diagnostic and therapeutic tool for clinical applications⁷. Thus, there is a broad range of potential applications and uses for EVs, namely as biomarkers, vaccines and drug delivery devices⁵.

1.2.1.3. Separation and concentration methods

The potential benefits and uses of EVs have been described above, however, a major hindrance in further progresses in the field of EVs is the lack of standardization in isolation methods⁵. It is imperative to isolate EVs from a wide range of cell fragments and interfering substances⁷ such as viruses, lipoproteins, and large protein aggregates². Depending on the source and size of EVs, different techniques can be adopted to separate them from body fluids or cell cultures⁷ and based on the principle of their separation, the isolation methods can be categorized into three major classes: (a) density, (b) size, and (c) immunoaffinity².

In order to select the isolation procedures for a specific application, several factors should be considered, such as sample nature, sample volume, the desired degree of purity and the final intended use for the isolated EVs¹. Depending on the extent of purity of an EV preparation and the concentration required for a certain application, a combination of isolation methods might be necessary to outperform single-method approaches¹³.

1.2.1.3.1. Density-based isolation

EVs can be separated upon centrifugation based on their density. The techniques include ultracentrifugation and centrifugation with precipitation reagents, including commercial kits (Table 1-2)². Although (ultra)centrifugation (coupled or not with precipitation reagents) is the most extended and standardized procedure, this method presents several technical limitations for its practical implementation from a clinical point of view¹.

Table 1-2 Separation of EVs based on density: ultracentrifugation and centrifugation with precipitation reagents^{1,2}

Technique	How it works	Advantages	Disadvantages
Ultracentrifugation	Separation by differential centrifugation by varying the g-force: cells and cellular debris are removed at a low g-force and EVs sediment at a high g-force	Conventional and most commonly used method; can process large sample volumes	Time-consuming, requires an ultracentrifuge, low recovery and can cause some damage to the EVs integrity
Centrifugation with precipitation reagents	The reagents reduce the solubility by lowering the hydration of EVs and lead to precipitation	EVs can be separated at a low g-force and with a higher yield than ultracentrifugation	Time-consuming, expensive and low purity of the EVs preparation

1.2.1.3.2. Size-based isolation

Based on the sizes of EVs, nano-sized membrane filters (with various pore sizes and materials) can be used to separate the EVs from cells and large debris, subcellular fractions, protein aggregates, protein-nucleic acid aggregates or plasma proteins². Filtration has been reported to be efficient, quick and able to achieve good results¹. However, this technique does not isolate the EVs subpopulations specifically but enriches them from a complex mixture of samples² and can only be performed with relatively small volumes¹.

1.2.1.3.3. Immunoaffinity-based isolation

Immunoaffinity-based methods allow a more specific isolation of EVs subpopulations¹ (cell culture, tissues and biological fluids) by exploiting the interaction between the surface proteins of EVs (antigens) and their antibodies, and specific interactions between receptors and their ligands¹⁵. Antibodies for a specific antigen of interest can be attached to plates (*e.g.*, enzyme-linked immunosorbent assay (ELISA)), magnetic beads, resins and microfluidic devices⁵. Due to the complexity of biological fluids, this method is often used after EVs enrichment by ultracentrifugation or ultrafiltration⁵.

A major benefit of these techniques is that they allow the isolation of EVs derived from a specific source⁵, are more rapid, easy, compatible with routine laboratory equipment, have no volume limitations and are more efficient than ultracentrifugation and density isolation methods¹⁵. Additionally, the immunoaffinity methods have the potential to isolate a specific sub-set of EVs from a complex mixture, and also to separate different types of EVs⁵.

The main limitation of this method is that the antibody can only capture the EVs by recognizing antigens expressed on their surface. Also, the specificity is limited to that of the antibody used, and this method results in a lower yield of isolated EVs with higher purity than the other methods discussed⁵.

1.2.1.4. Characterization

The potential use of EVs in the clinical setting depends not only on the standardization of isolation methods but the characterization of EVs must also be improved. In this sense, to determine their biological functions, the accurate determination of the physicochemical (size and surface charge) and biochemical (molecular cargo of proteins, nucleic acids, and lipids) properties is of the utmost importance. Likewise

the isolation methods, researchers also combine several characterization techniques to overcome the limitations of each individual method when applied to study such vesicles at the nanoscale¹⁵.

1.2.2. Biosensors

Biosensors combine a biorecognition element with a signal processor and a suitable transducer approach, which can be of electrochemical, mass, or optical nature, among others¹⁶, for detecting substances and monitoring biological interactions¹⁷. The biobased recognition element includes a capture compound (mostly antibodies or enzymes) that bind to/interact selectively with the target analyte. The use of antibodies and enzymes as capture compounds provide selective molecular recognition, however, they have a lower stability. For this reason, it's crucial the development of synthetic biorecognition elements, such as molecularly imprinted polymers (MIPs)¹⁶.

1.2.2.1. Biorecognition using MIPs

MIPs are tailor-made synthetic materials with artificially generated recognition sites able to specifically rebind a target compound in preference to other closely related compounds¹⁸. Compared to other recognition systems, MIPs possess three major unique features, such as the structure predictability, the recognition specificity, and the application universality. These properties make their application attractive in many fields, such as purification and separation, chemo/biosensing, drug delivery, and catalysis, owing to their high physical stability in comparison with antibodies¹⁶, straightforward preparation, remarkable robustness and low cost¹⁹.

1.2.2.1.1. MIP synthesis

MIPs are obtained by polymerizing functional and cross-linking monomers around a template molecule, leading to a highly crosslinked three-dimensional (3D) network polymer¹⁸. The structure of the polymer matrix is macroporous with nanocavities complementary to that of the template molecule, which is the most important factor of molecular recognition²⁰. The monomers are chosen based on their capability to interact with the functional groups of the template molecule¹⁸. The scheme of the molecular imprinting process is presented in Figure 1-4.

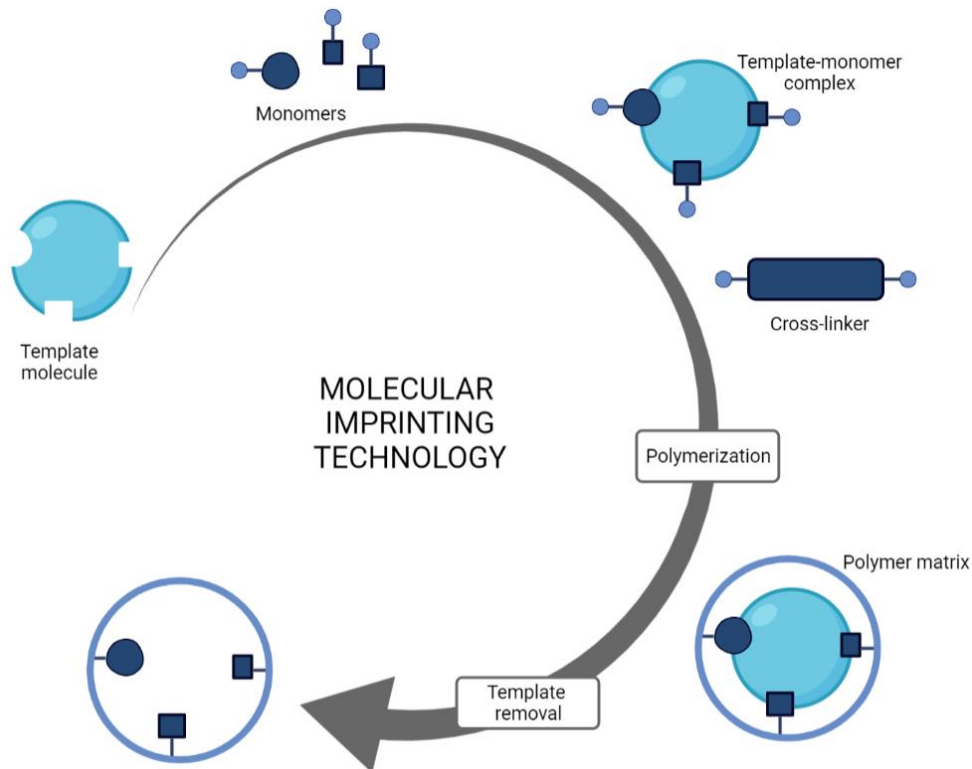


Figure 1-4 Scheme of the molecular imprinting process.

- › Polymerization: the first step of the process relates to the dissolution of template, functional monomer, cross-linker, and initiator in a porogenic solvent. The functional monomer interacts with the template molecule, which results in the formation of a stable template-monomer complex. Functional monomers are positioned around the template molecule and are fixed by copolymerization with cross-linkers²⁰;
- › Template removal: the next step involves removal of the template molecule for example by solvent extraction²⁰. The polymer matrix is left with binding sites complementary in shape, size and functionalities to the target compound¹⁸. Therefore, the obtained polymer matrix recognizes and binds selectively the template molecules²⁰.

The resulting imprinted polymers are stable, robust, and resistant to a wide range of pH, solvents, and temperature. Therefore, the behaviour of MIPs mimics the interactions established by natural receptors to selectively retain a target molecule, but without the associated stability limitations. In addition, the synthesis of MIPs is relatively simple and inexpensive, providing an excellent alternative to the use of

natural receptors¹⁸. Three general approaches have been described for the synthesis of MIPs, namely, covalent, non-covalent, and semi-covalent approaches (Figure 1-5).

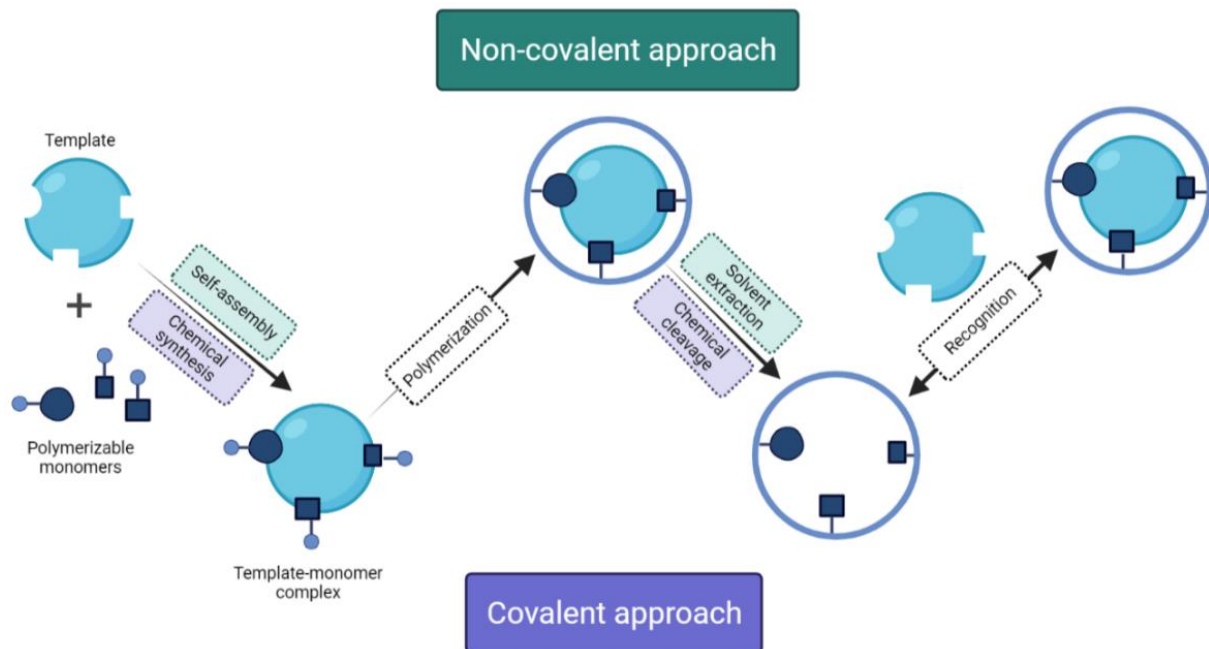


Figure 1-5 Approaches for the synthesis of MIPs.

Covalent approach:

The covalent approach involves the formation of reversible covalent bonds between the template molecule and monomers before polymerization. Then, the template is removed from the polymer by cleavage of the corresponding covalent bonds, which are formed again upon rebinding of the target compound¹⁸. Covalent imprinting, being stoichiometric, ensures that functional monomer residues exist only in the imprinted cavities. This method often uses readily reversible condensation reactions involving boronate esters, ketals/acetals and Schiff's base¹⁹. Furthermore, this approach leads to homogeneous binding sites within the polymer, minimizing the existence of non-specific sites due to the high stability of template-monomer interactions¹⁸. However, the covalent approach is less flexible¹⁹ due to the difficulty of designing appropriate template-monomer complexes in which readily reversible covalent bond formation and cleavage occur under mild conditions¹⁸. Moreover, it is very difficult to reach thermodynamic equilibrium since the strong covalent interactions results in slow binding and dissociation¹⁹.

Non-covalent approach:

The non-covalent approach is based on the formation of relatively weak non-covalent interaction (hydrogen bonds, ionic interactions, Van der Waals forces and $\pi - \pi$ interactions¹⁹) between the template molecule and selected functional monomers before polymerization and, most commonly, the dominant interaction is hydrogen bonding^{18,19}. This approach is by far the most common for the preparation of MIPs owing to its simplicity of operation and rapidity of binding and removal¹⁹, as well as the availability of a wide variety of monomers¹⁸. However, the non-covalent imprinting is less robust because it is sensitive to even slight disruption of the interactions holding the complex together¹⁹.

Semi-covalent approach:

The durability of covalent imprinting and the rapid target uptake of non-covalent imprinting can be combined in the semi-covalent imprinting method¹⁹, offering an alternative intermediate approach¹⁸. In this case, the template is also covalently bound to a functional monomer, but the template rebinding is based only on non-covalent interactions¹⁹.

1.2.2.1.2. Application of MIPs for the recognition of EVs

To the best of knowledge, there are only two published works on biosensors for EVs that complement the use of antibodies with MIPs^{21,22}. The first reported a novel fluorescence-based sensing prepared by molecular imprinting and post-imprinting modifications. These modifications were made only inside the recognition cavities and consisted in introducing antibodies and fluorescent reporter molecules. By using this methodology, the authors demonstrated the differentiation of cancer-secreted EVs from normal ones by a rapid and highly sensitive fluorescent sensing, avoiding time-consuming pre-treatments such as ultracentrifugation²¹. In the second, a nanocavity-based platform was designed by using silica nanoparticles as a dynamic mould and the molecular imprinting approach together with antibody-conjugated signalling. This tool can be successfully applied to diagnose various types of cancer and infectious diseases by customizing the dynamic moulding sizes and antibodies²².

1.2.2.2. Optical detection based on photonic crystals

Optical biosensors have been extensively studied because they exhibit excellent analytical performances in detecting a wide range of analytes, including biological targets, which make them very

useful for promoting significant advances in clinical diagnostics and in drug discovery²³. Thus, optical biosensors offer great advantages over conventional analytical techniques: they enable direct, real-time and label-free detection of many substances¹⁷. Additional features include the absence of sample pre-treatment for reliable, and highly sensitive and selective responses. The possible miniaturization and lowering the costs enhances the potential portability and integration on microfluidic chips and arrays.

An approach for developing optical biosensors is based on photonic crystals (PhCs). PhCs are composed of a periodic arrangement of regularly shaped materials with different dielectric constants²⁴, with the properties of confining and controlling the propagation of light²⁵. Owing to the periodicity in dielectric, these materials exhibit a photonic band gap (PBG), which is a band of frequencies in which light propagation in the PhC is forbidden and is thus reflected^{25,26}. The reflection maximum (or transmission minimum) can be shifted by varying the angle of incidence, the lattice spacing or material composition²⁶. These observations are described by the Bragg-Snell's law (Equation 1-1). m is the order of the Bragg diffraction; λ is the wavelength of the reflected light; d is the diffracting plane spacing; n_{eff} is the effective refractive index; θ is the angle of light incidence.

$$m\lambda = 2d\sqrt{n_{\text{eff}}^2 - \sin^2\theta}$$

Equation 1-1

The Bragg-Snell's law can, therefore, describe the colourful PhC materials. PhCs exist throughout the natural world, from opal gemstones and beetles, to bird feathers and butterfly wings, and the common characteristic between all is their iridescent colour^{27,28}. This colour that changes depending on angle of observation, does not arise from any absorption or pigmentation alone but is instead caused by the interaction of light with the periodic architecture of these materials natural design^{27,28}, as described by the Bragg-Snell's law, being also referred to as "structural colour".

Structural colour are colours caused by the physical structure of a material, rather than the chemical molecules of conventional dyes and/or pigments²⁹, and can be classified as iridescent or non-iridescent: if the colour changes with the viewing angle it is called iridescent colour, while non-iridescent colours remain similar in appearance regardless of the angle of observation³⁰. Considering the physical mechanisms, both interference and diffraction can produce iridescent colours, and some forms of scattering originating from the irregularity of the structures produce non-iridescent colours³⁰. Compared to colours from traditional dyes and pigments, structural colour has several advantages including: high intensity, resistance to fading, easy tunability of colours, environmental friendliness, and less toxicity, as

the raw materials for producing structural colours are normally colloidal particles such as silica or polymers spheres²⁹. Furthermore, because the PBG is located in the visible light region, the structural colour of the PhCs can be directly observed by the naked eye without the need of expensive equipment to read the signals²⁴. Therefore, because of these unique characteristics, the potential applications of PhCs are highly prospective, such as biochemical sensing²⁵, optical filters²⁵, photonic papers²⁵, inkless printing²⁵, photovoltaic devices²⁴, reflective flat displays^{24,25} and so on.

PhCs can be divided in three types of structures: one-dimensional (1D), two-dimensional (2D) and 3D²⁴ (Figure 1-6). Particularly, 3D PhCs periodicity potentially manipulates the flow of light in all directions²⁴, and if it possess a sufficiently high refractive index ratio, suitable periodicity, and a dielectric filling ratio, a full gap might be formed²⁵. For these reasons, the 3D PhCs are considered to be one of the most potential materials²⁵, attracting much attention in the fields of biomolecule detection, real-time monitoring of enzyme activity, cell morphology research, among others²⁴. The most exploited configurations of 3D structures are opal systems (both direct or inverse), due to their low cost, flexibility, and power free analysis³¹.

Artificial opals are multilayers of colloids arranged in close-packed lattices and are called like this in analogy to natural opal stones. Colloidal spheres of silica, polystyrene (PS) and poly(methyl methacrylate) (PMMA) are commonly used to construct such PhCs and their sizes are in the same length scale of the wavelengths of visible light³².

It is also very common to use the opal structures as sacrificial template to originate inverse opal structures as negative replicas of the opals. The photonic matrix is filled with a dielectric material and spheres are subsequently removed. Inverse opals can present a complete PBG, however, this requires a high refractive index contrast. They possess large voids due to their inner structure, *i.e.*, a great surface area with plenty potential interaction sites and a great access of the analyte to the recognition sites³³.

Fabrication of synthetic PhCs can be usually classified into two main categories: top-down and bottom-up. These two general classifications can be distinguished based on the process that is used to create the nanometer-sized structures³⁴. Top-down techniques have dominated the fabrication of PhCs, but recent advances in bottom-up assembly approaches demonstrated their scalability to produce large arrays of homogeneous nano-patterned surfaces and materials. In addition, bottom-up assembly methods are relatively low cost when compared to top-down fabrication approaches, which is a great advantage³⁵.

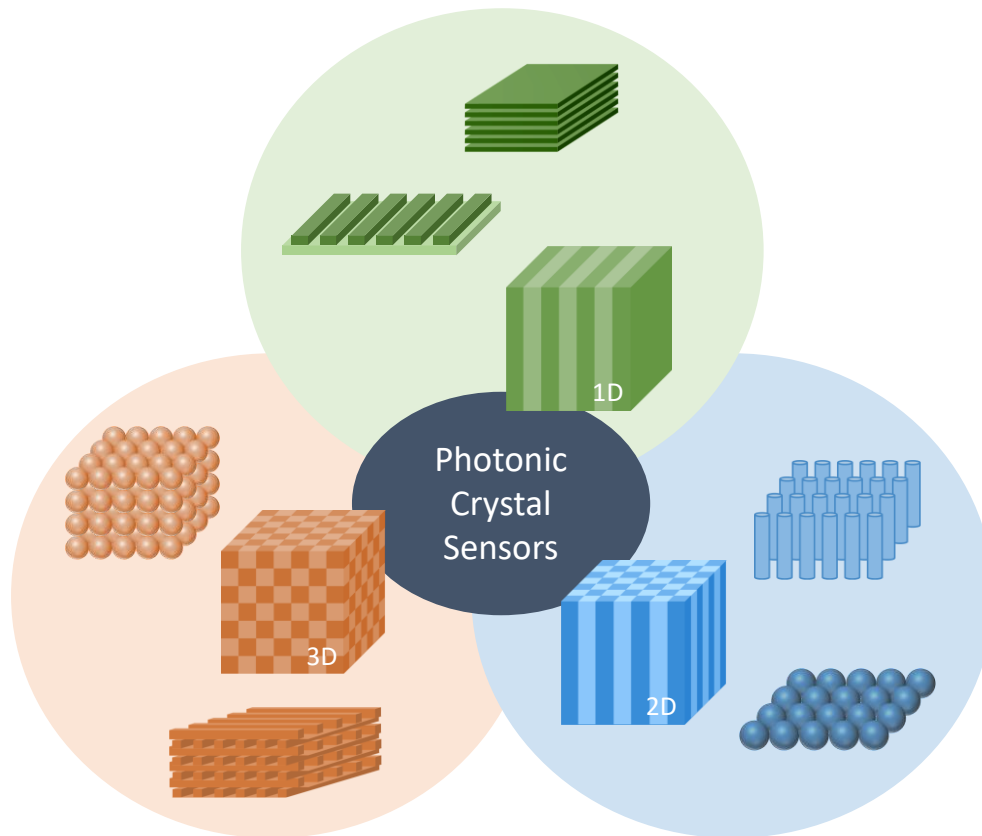


Figure 1-6 Photonic sensors are developed as 1D, 2D or 3D structures in several configurations.

› **Top-down:**

In the top-down fabrication, the base material is gradually eroded until the desired shape is achieved, *i.e.*, nanostructures are produced by deconstructing larger materials. Top-down approaches offer high precision and resolution to the final structure of the PhC. However, they are generally expensive and the fabrication of structures over a larger area is very time-consuming³⁵.

Several lithography-based methods are commonly used as top-down approaches (*e.g.*, optical, E-beam, nanoimprint and block co-polymer lithographic techniques)³⁶. These methods present main advantages like versatility in terms of symmetry of the fabricated structure and the ability to introduce designed defects, crucial for many applications³⁷. Their main drawbacks are the high costs, the large time scales required for the fabrication processes³⁷ and the difficulty of precise alignment for lithography and etching steps in the nanometer scale³⁸.

› **Bottom-up:**

The bottom-up approach relies on the self-driven assembly of the building blocks that will compose the desired ordered periodic nanostructures. These methods still face some challenges related to the control of impurities, site uniformity, *etc.*³⁶. Nonetheless, these difficulties in the control and precision of the fabricated structures are largely surpassed by their clear advantages in comparison to top-down approaches. The bottom-up approaches are generally simple, fast, easy to fabricate and cheap, offering a viable alternative to also produce structures on a large scale^{35,39}.

The bottom-up approaches are commonly used in the fabrication of 2D and 3D PhCs, using spherical colloids (*e.g.*, silica, PS or PMMA) as building blocks for assembly. In colloidal assembly there are three types of forces that bring these building blocks together³⁵: (1) intrinsic driving forces for ordering, and in the case of colloids could be the entropically favourable packing into ordered arrays, thus the monodispersity of the particles (size and shape homogeneity) is crucial; (2) long range external forces (gravity and centrifugation) act to bring the particles together; (3) repulsion forces between particles (electrostatic and steric repulsions) that prevent their early aggregation arising from Van der Waals forces³⁵.

There is a variety of assembly methods available for the fabrication of colloidal crystals, which can be chosen according to the type of building blocks, the final design of the structure and the intended application³⁵ (Table 1-3).

Table 1-3 Methods commonly used for colloidal assembly⁴⁰⁻⁵⁶

Method	How it works	Advantages	Disadvantages
Drop casting	The colloidal suspension is dropped onto a flat surface followed by evaporation of the solvent	Simple, easy and rapid	Patches of colloidal crystals formed and the exact conditions are difficult to control

Table 1-3(Continuation) Methods commonly used for colloidal assembly⁴⁰⁻⁵⁶

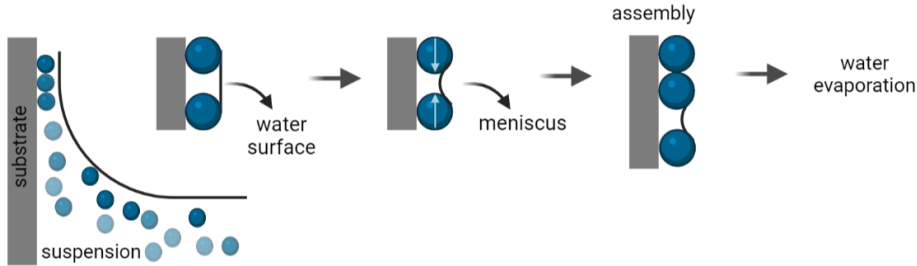
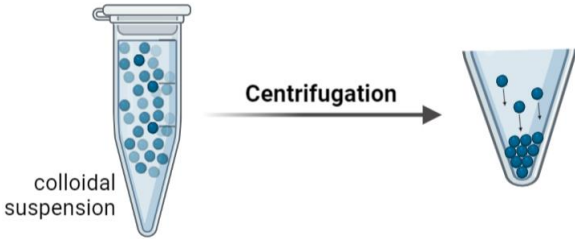
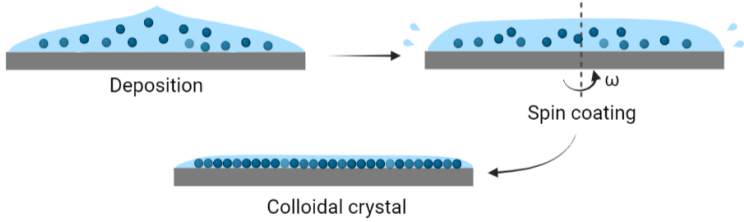
Method	How it works	Advantages	Disadvantages
<p>Vertical deposition</p>	<p>The substrate is placed vertically in the colloidal suspension and is gradually exposed as the solvent evaporates</p>	<p>Uniform films with well-defined shape and control of the crystal structure and thickness</p>	<p>Slow process (days)</p>
	 <p>The diagram illustrates the vertical deposition process in four stages. 1. A substrate is partially submerged in a colloidal suspension. 2. The substrate is moved up, creating a meniscus in the suspension. 3. The substrate is further moved up, and particles begin to assemble on its surface. 4. The substrate is fully out of the suspension, and the particles on its surface undergo water evaporation to form a film.</p>		
<p>Centrifugation</p>	<p>The colloidal suspension is placed in a centrifuge and spun at high speeds to bring the particles together resulting in bulk colloidal crystals</p>	<p>Robust and flexible enough films to be easily transferred on various planar and curved substrates</p>	<p>The products are considerably less ordered</p>
	 <p>The diagram shows a test tube containing a colloidal suspension. An arrow labeled 'Centrifugation' points to the test tube after spinning, where the particles have settled at the bottom, forming a dense layer.</p>		
<p>Spin-coating</p>	<p>The centrifugal force drives the solution to spread in a thin film where the solvent rapidly evaporates to produce a uniform coating layer on the substrate</p>	<p>Simple and fast, with the possible formation of monolayers</p>	<p>It's difficult to accurately control the deposition</p>
	 <p>The diagram shows the spin-coating process in three stages. 1. 'Deposition': A substrate is coated with a thick layer of colloidal suspension. 2. 'Spin coating': The substrate is rotated at angular velocity ω, spreading the suspension into a thin, uniform film. 3. 'Colloidal crystal': The solvent evaporates, leaving a uniform, ordered layer of colloidal particles on the substrate.</p>		

Table 1-3(Continuation) Methods commonly used for colloidal assembly⁴⁰⁻⁵⁶

Method	How it works	Advantages	Disadvantages
Dip-coating	Immersion of the substrate into the colloidal suspension and its withdrawal at constant speed	Simple, low-cost, reliable, reproducible, and the thickness is controlled by the speed of withdrawal	Slow process
Langmuir-Blodgett	Particles compressed on the water surface are transferred to a substrate by mobile arms	Well-established, simple and sophisticated method, producing highly ordered monolayers over large areas	Time-consuming (preparation of equipment and spreading of particles) and special equipment is required
Direct assembly on water surface	The close-packed monolayer directly forms at the air-water interface and can be transferred to substrates by immersion of the substrate into the water phase and picking up the monolayer with a transfer substrate	Simple, highly configurable, scalable and reproducible process, can be repeated to deposit multilayers exactly as desired and produces high quality colloidal monolayers over large areas	The films fabricated by this method are usually ultrathin, their adhesion to the desired substrate is weak, and the morphology is not well-ordered

1.2.2.3. Molecularly imprinted photonic polymers

Despite the many advantages of MIPs, like high selectivity and strong affinity, there are still some drawbacks, such as the difficulty in transforming the binding event into a detectable optical signal²⁴. A very promising strategy is the combination of PhCs with the molecular imprinting technique, resulting in molecularly imprinted photonic polymers (MIPPs) sensors. These sensors have the advantage of directly convert the molecular recognition process into a measurable optical signal.

For instance, the PhC can be incorporated into hydrogel polymers, that can swell or shrink in response to different stimuli, and lead to changes in the reflection wavelength sometimes accompanied by a visually colour change, making them very promising in label-free detection of different analytes²⁴. Therefore, photonic biosensors with MIPs can enable a direct detection of the analyte *via* a change of polymer conformation upon the selective recognition of the target molecule³³. Table 1-4 lists examples of MIPPs that have been developed.

Table 1-4 Examples of MIPPs: target molecule, spheres used as PhC template, self-assembly method, and PhC's final design in the photonic sensor⁵⁷⁻⁸¹

Target	Spheres	Colloidal assembly	PhCs design	Ref.
L-DOPA	silica	vertical deposition	inverse opal	57
bovine serum albumin	silica	vertical deposition	inverse opal	58
theophylline and (1R,2S)-(S)-ephedrine	silica	vertical deposition	inverse opal	59
cholic acid	silica	vertical deposition	inverse opal	60
atrazine	silica	vertical deposition	inverse opal	61
bisphenol A	silica	Langmuir–Blodgett	inverse opal	62
cholesterol	silica	vertical deposition	inverse opal	63
levodropropizine	silica	vertical deposition	inverse opal	64
bisphenol A	silica	Langmuir–Blodgett	inverse opal	65
bisphenol A	PMMA	vertical deposition	opal	66
methyl phosphonic acid	PMMA	vertical deposition	opal	67
vanillin	silica	vertical deposition	inverse opal	68
tetracycline	PS	vertical deposition	inverse opal	69
creatinine	silica	vertical deposition	inverse opal	70
chloramphenicol	silica	vertical deposition	inverse opal	71

Table 1-4(Continuation) Examples of MIPPs: target molecule, spheres used as PhC template, self-assembly method, and PhC's final design in the photonic sensor⁷²⁻⁸¹

Target	Spheres	Colloidal assembly	PhCs design	Ref.
atropine	silica	vertical deposition	inverse opal	72
ketamine	silica	vertical deposition	inverse opal	73
imidacloprid	silica	vertical deposition	inverse opal	74
glucose	PMMA	vertical deposition	inverse opal	75
L-pyrogutamic acid	PS	vertical deposition	inverse opal	76
L-proline	PS	vertical deposition	inverse opal	77
L-tryptophan	PS	vertical deposition	inverse opal	78
cinchonine	PS	vertical deposition	inverse opal	79
testosterone	silica	vertical deposition	inverse opal	80
oxytetracycline	PS	assembly on water surface	opal	81

1.3. Objectives of the thesis

EVs have a huge potential as biomarkers of disease and health, but improved methods for their separation, concentration and detection are crucial to overcome the hurdles faced due to their heterogeneity and nanosizes, as well as the complexity of the biofluids where EVs circulate. Thus, the main goal of this work was to introduce a novel technology to isolate and detect EVs. To this end, the aims were:

Aim 1 > Fabricate a novel hydrogel-based MIPP for CD9 surface protein of EVs

Colloidal spheres were synthesized, self-assembled as photonic structures, and incorporated into a hydrogel molecularly imprinted with the CD9 protein. All materials were properly characterized.

Aim 2 > Analyze the analytical performance of the sensor for CD9 recognition

The recognition of CD9 protein by the sensor was tracked by an optical signal. The studies were performed in various matrices to determine the sensitivity, selectivity, and limit of detection (*LOD*) of the sensor.

Aim 3 > Investigate the response of the sensing material to EVs

The sensor ability to recognize a range of EV concentrations was studied in order to access its potential as alternative to conventional isolation methods.

Chapter 2. Materials and methods

In this work, a variety of methods and techniques were applied and optimized for the opal structure construction (*e.g.*, dip coating and vertical deposition), as well as the photonic hydrogel construction (*e.g.*, photopolymerization). However, the reported methods and techniques in this work were the ones that showed more promising results. The chosen design for sensor fabrication involves several steps that are schematically depicted in Figure 2-1.

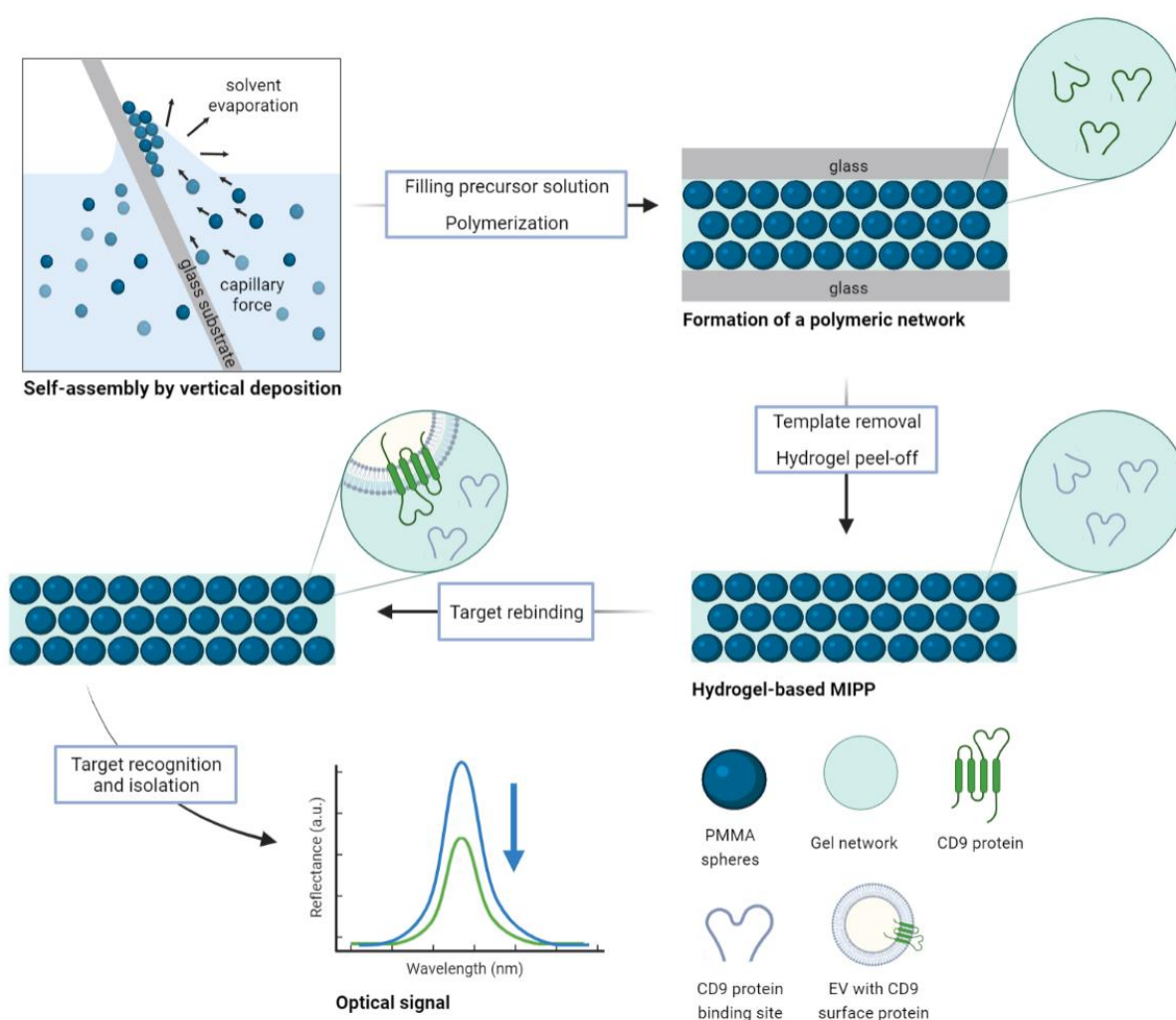


Figure 2-1 Sensor construction involves the synthesis of monodisperse PMMA colloidal spheres and their self-assembly on glass substrates, preparation of hydrogel-based MIP for CD9 protein and study the analytical response of the MIP sensor towards CD9 protein and the recognition ability of EVs.

2.1. Reagents

All chemicals were of analytical grade and used without further purification. Acrylamide (AAm), *N,N'*-methylenebisacrylamide (Bis-A), phosphate-buffered saline (PBS) buffer, *N,N,N',N'*-tetramethylethylenediamine (TEMED) and methyl methacrylate (MMA) were from Merck Sigma-Aldrich. Potassium persulfate (KPS) and nitric acid 65 % were from Honeywell Fluka. Acetone 99.5 % and ethanol 99.8 % were from Honeywell Riedel-de Haën. 2-hydroxyethyl methacrylate (HEMA) was from Alfa Aesar. Recombinant human proteins CD9 (UniProt: P21926; Recombinant protein fragment of approximately 11kDa) and CD81 (UniProt: P60033; Recombinant protein fragment of approximately 12 kDa) were from Abcam and recombinant GLAST-1 protein (UniProt: P43003; Recombinant protein fragment of approximately 11 kDa) was from Cusabio. The control serum used in this work was lyophilized human serum, CORMAY SERUM HN from PZ Cormay S.A. EVs isolated from primary human astrocyte cells were kindly provided by the laboratory of Professor Seppo Vainio from the University of Oulu (partner of MindGAP project). Ultrapure laboratory grade water conductivity ($\kappa < 0.1 \mu\text{S cm}^{-1}$) was employed throughout.

2.2. Synthesis of PMMA colloidal spheres

The 3D PhC used in this work for the construction of the photonic hydrogel was obtained through a bottom-up approach, where PMMA colloidal spheres were self-assembled as PhC building blocks. Among the most widely used materials that could be used for this purpose (*e.g.*, silica, PS and PMMA), PMMA spheres were the ones selected in this work, due to the various reported properties of this polymer, namely its good thermal stability, interesting optical properties, and high resistance to scratching⁸². The successful fabrication of opals with good reproducibility is highly dependent on the ability to prepare monodisperse colloidal spheres with controlled size so that the spheres self-assemble into ordered matrices with a defined structure⁸². Accordingly, a surfactant-free emulsion polymerization method was used for the synthesis of spherical, uniform, porous and monodisperse PMMA colloidal spheres with a certain size and clean surface features. In this method, the only monomer (MMA) is dispersed in ultrapure water and, in the presence of a thermo initiator (KPS), the free radical polymerization is initiated. Furthermore, using this method, the synthesis conditions (temperature, stirring speed and amounts of monomer and initiator) are key factors that influence the particle size. In this sense, a precise protocol was followed: a solution of 1.10 mol L^{-1} of MMA in ultrapure water was first prepared inside a three-necked round-bottom flask equipped with a reflux system, which was purged with nitrogen. Then,

$1.80 \times 10^{-3} \text{ mol L}^{-1}$ of KPS was added to the solution under stirring (300 rpm), and the system was once again purged using nitrogen and closed, beginning the reaction process, which lasted 2 h at a constant temperature of $100 \text{ }^\circ\text{C}$. Once the reaction was complete, the obtained colloidal suspension was allowed to cool to room temperature before starting the cleaning procedure. The PMMA suspension was subjected to several rounds of centrifugation at 500 rpm for 30 min, where the supernatant was discarded, and the pellet was redispersed in ultrapure water.

2.3. Opal construction

As illustrated in Table 1-3, there are many techniques that can be employed for the formation of a PhC matrix by the self-assembly of colloidal spheres. In this present work, the one that showed more promising results was the vertical deposition. To achieve this result, small transparent glass vials and thin glass slides ($1.1 \text{ cm} \times 2.5 \text{ cm}$) were thoroughly cleaned with a rigorous washing procedure of successive 15 min sonication with nitric acid 65 %, acetone 99.5 % and ethanol 99.8 % (with 15 min sonication with ultrapure water in between). Each dried vial was filled with 3 mL of the PMMA colloidal suspension (dispersed in ultrapure water) with, approximately, 1 mg mL^{-1} , and the glass substrate was placed into the suspension with an angle of approximately 25° , as illustrated in Figure 2-2. Finally, the vial was placed in a muffle furnace at $60 \text{ }^\circ\text{C}$ for at least 40 h to allow the solvent to evaporate, and, as a result, during the solvent evaporation, the PMMA colloidal spheres spontaneously form a close-packed array on the glass substrate.

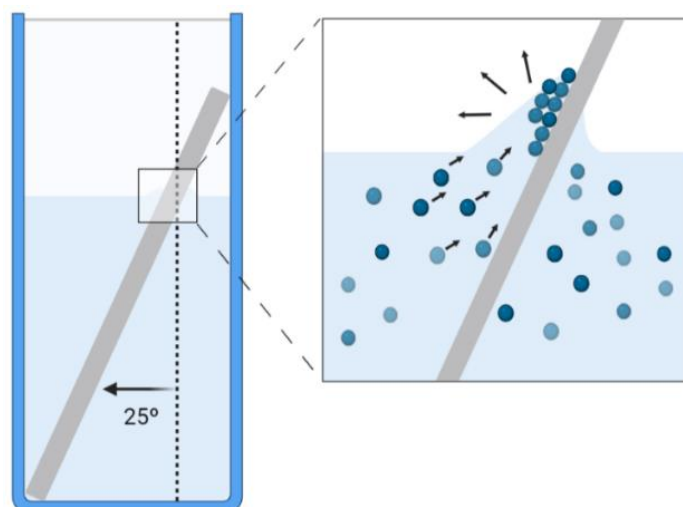


Figure 2-2 Schematic illustration of the vertical deposition process. PMMA colloidal spheres self-assemble by solvent evaporation and form a PhC film.

After self-assembly, as the opal film dries, PMMA spheres coalesce and shrink. This decrease in volume upon drying and the presence of unconverted MMA in dispersions may promote the formation of bridges between the spheres⁸³. In order to increase the sphere-to-sphere contact area, called the neck, as can be seen highlighted in Figure 2-3, and, therefore, enhance the structural integrity of the opal film⁸⁴, an annealing process was performed during 15 min at 90 °C.

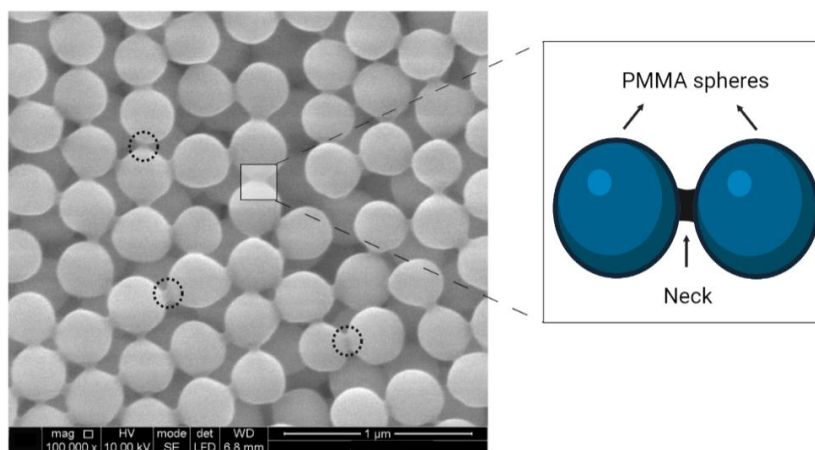


Figure 2-3 Schematic representation of the formation of bridges between adjacent PMMA spheres.

2.4. Hydrogel-based MIPP for recognition of CD9 protein

Once the opal film was obtained, the hydrogel precursor solution was infiltrated into the interstitial space of the opal by capillary forces and underwent a free radical polymerization to construct an embedded PMMA colloidal array within the hydrogel network, where the crystalline lattice of the opal was permanently captured. The pre-polymeric solution used to form the hydrogel was prepared using $3.29 \mu\text{g mL}^{-1}$ of the tetraspanin CD9 fragment protein as template, 1.05 mol L^{-1} of AAm and $3.24 \times 10^{-1} \text{ mol L}^{-1}$ of HEMA as functional monomers, $4.90 \times 10^{-2} \text{ mol L}^{-1}$ of Bis-A as cross-linker and $8.76 \times 10^{-3} \text{ mol L}^{-1}$ of TEMED and $1.31 \times 10^{-3} \text{ mol L}^{-1}$ of KPS as the reaction initiators. A second clean glass slide was placed and held firmly on top of the colloidal crystal, forming a “sandwich structure”, and the pre-polymeric solution was introduced and infiltrated into the interstitial spaces in the opal film by capillary force. After 2 h at room temperature, the polymerization was complete and the obtained hydrogel-based MIPP was rinsed and stored in ultrapure water for 1 h to hydrate. The CD9 protein template and unreacted reagents were removed using a solution of ethanol 25 % through incubation for 3 h, obtaining a MIPP of

the CD9 protein. The hydrogel-based MIPP was rinsed and stored in ultrapure water before any other analysis. A non-imprinted photonic polymer (NIPP) was used as control, where the CD9 protein was substituted by 3.29×10^{-4} mol L⁻¹ of PBS buffer with a pH = 7.4.

2.5. Characterization of the sensing materials

The PMMA colloidal spheres were characterized by attenuated total reflectance-Fourier transform infrared spectroscopy (ATR-FTIR; Nicolet™ iS20, Thermo Fisher Scientific, Waltham, Massachusetts, USA) in transmittance mode with a Thermo Scientific Smart iTX accessory equipped with a diamond crystal and using a scanning range of 400 cm⁻¹ – 4000 cm⁻¹ for 250 scans, at a spectral resolution of 4 cm⁻¹. Prior to scanning electron microscopy (SEM) analysis the samples were sputter coated with a thin film of Au/Pd. The surface morphology of the PMMA spheres, as well as the surface and cross-section morphology of the opal and MIPP were analysed by scanning electron microscopy (SEM; FEI Quanta 400FEG ESEM, Hillsboro, Oregon, USA). The diameter of the PMMA spheres was determined and characterized using two techniques: from the SEM micrographs considering 50 spheres and using the ImageJ software, and by dynamic light scattering (DLS; Malvern Zetasizer Nano ZS, Malvern Instruments Worcestershire, UK). With the DLS system was also possible to measure the polydispersity index (PDI) and the zeta potential from the diluted colloidal suspension. The size, PDI and zeta potential data of the PMMA spheres were obtained directly from the equipment software, where three consecutive measurements at 20 °C were taken, and the reported values are average values of those measurements. The optical characterization of the opal film and MIPP was performed using an optical set-up: a reflection fiber probe (fiber diameter of 400 μm, Sarspec, Portugal), a visible light source (DWHP light source, Sarspec, Portugal) and a spectrophotometer (spectrometer FLEX RES+ UV/Vis, Sarspec, Portugal), where a diffuse reflectance standard was used as a reference surface and the reflectance at 45° was collected using the optical fiber probe.

2.6. Sensing ability of the hydrogel-based MIPP towards the CD9 protein

The recognition ability of the hydrogel-based MIPP towards the CD9 protein and the analytical performance of the photonic sensor was assessed through calibrations experiments. The reflectance spectra were collected after incubating the sensor with increasing concentrations of CD9 standards and a calibration curve was constructed. The calibration curve translates the relationship between the sensor

signal response and the known analyte concentrations. The purpose is to demonstrate the ability of the sensor to recognize the target biomarker (CD9 protein), relying on the high affinity recognition cavities in the MIP material. After the assembly of the hydrogel and before the calibrations, the hydrogel was incubated in PBS buffer ($1.00 \times 10^{-2} \text{ mol L}^{-1}$, pH 7.4) for 30 min, several times, until a stable response was obtained, suggesting that the sensor is equilibrated and ready for the calibration experiments. Afterwards, the sensor was incubated for 30 min with successive increasing concentrations of CD9 protein ($25 \text{ pg mL}^{-1} - 5859 \text{ pg mL}^{-1}$) in PBS buffer. The range of concentrations was chosen bearing in mind the range of concentrations that can be detected in a typical ELISA, in order to prove that the biosensor developed in this work has a similar linear range when compared to the common tools used for the detection of the CD9 protein. With the obtained data, the hydrogel-based MIPP sensor response to the CD9 protein was analysed by I/I_0 , where I correspond to the maximum intensity of the reflectance peak and I_0 the maximum reflectance peak intensity of the control spectrum ($[\text{CD9}] = 0 \text{ pg mL}^{-1}$). Calibration plots of the optical signal (I/I_0) against the logarithm concentration of CD9 were evaluated with regard to the linear regression obtained. The next step required the evaluation of the sensor ability to detect the same range of concentrations of the CD9 protein ($25 \text{ pg mL}^{-1} - 5859 \text{ pg mL}^{-1}$) in a more complex matrix, human serum. All the studies in serum were performed after 1000-fold dilution in PBS buffer, and the obtained results were analysed in the same manner as the ones in PBS buffer. The calibration plots were analysed to calculate the LOD and the slope of the curves enabled to compare the sensitivity of the sensor in both tested matrices. The LOD is defined as the lowest concentration of a substance in a sample that can be distinguished from the absence of that substance (a blank value) within a stated confidence limit⁸⁵⁻⁸⁷. Herein, $LODs$ were calculated as the concentration taken at the point of intersection of the fitted linear curve (at the minimum 95 % confidence limit) and a line parallel to the x-axis through the mean intensity value measured in the lowest concentration⁸⁸. To conclude, the serum (diluted 1000-fold) was spiked with known concentrations of the CD9 protein (90 pg mL^{-1} and 690 pg mL^{-1}) and the corresponding reflectance signal was analysed aiming to determine the accuracy of the sensor expressed as percent error. The formula for this calculation is given by Equation 2-1. $\%_{\text{error}}$ is the percent error, m_{value} is the measured value and exp_{value} is the expected value.

$$\%_{\text{error}} = \left| \frac{m_{\text{value}} - exp_{\text{value}}}{exp_{\text{value}}} \right| \times 100 \%$$

Equation 2-1

All the experiments were performed at room temperature and each condition was also tested on hydrogel-based NIPP as control, all in triplicate.

2.7. Recognition ability of the hydrogel-based MIPP towards EVs

Once the analytical performance of the sensor towards the CD9 protein was completed successfully, it was possible to proceed and test the sensor ability to recognize EVs isolated from astrocyte cells. As previously, the hydrogel was incubated in serum repeatedly, until a stable response was obtained and, afterwards, it was incubated for 30 min with successive unitary concentrations of EVs, ($6.85 \times 10^1 \mu\text{L}^{-1}$, $6.85 \times 10^3 \mu\text{L}^{-1}$ and $6.85 \times 10^5 \mu\text{L}^{-1}$) prepared in serum (diluted 1000-fold). The obtained response was analysed by *I/I₀* and statistical differences were evaluated using one-way analysis of variance (ANOVA), followed by linear trend analysis. Statistically significant differences were considered when $p \leq 0.05$. The experiments were performed at room temperature and hydrogel-based NIPP was used as control. All assays were performed in triplicate.

2.8. Selectivity studies by testing CD81 and GLAST-1 proteins

In order to determine if the EVs were being recognized through the CD9 protein and not by other surface-membrane protein, selectivity studies were performed using two different proteins present in the EVs: the CD81 protein, also a tetraspanin commonly found in EVs and GLAST-1 protein present in EVs derived from astrocytes⁸⁹. In this sense, the selectivity of the MIPP for the CD9 protein in serum (diluted 1000-fold) was examined against two CD81 protein concentrations (100 pg mL^{-1} and 1000 pg mL^{-1}). Once again, the MIPP sensor was incubated in serum repeatedly, until a stable response was obtained and, afterwards, it was incubated for 30 min with the two CD81 protein concentrations previously indicated. A similar selectivity study was performed by testing two concentrations of GLAST-1 protein (100 pg mL^{-1} and 1000 pg mL^{-1}). The experiments were performed at room temperature and all conditions were also tested on hydrogel-based NIPP as control. The obtained responses were analysed by *I/I₀* and all assays were performed in triplicate.

Chapter 3. Results and discussion

3.1. Characterization of the PMMA colloidal spheres

3.1.1. ATR-FTIR analysis

The successful synthesis of PMMA was confirmed by the analysis of the ATR-FTIR spectrum, shown in Figure 3-1, which provides a structural fingerprint by which molecules can be identified. The PMMA chemical structure contains an ester group, one methylene (CH_2) group and two methyl (CH_3) groups. Therefore, the bands present in the spectra correspond to vibrational modes of these groups, confirming that the polymerization process was successful, *i.e.*, the PMMA polymer was indeed synthesized⁸².

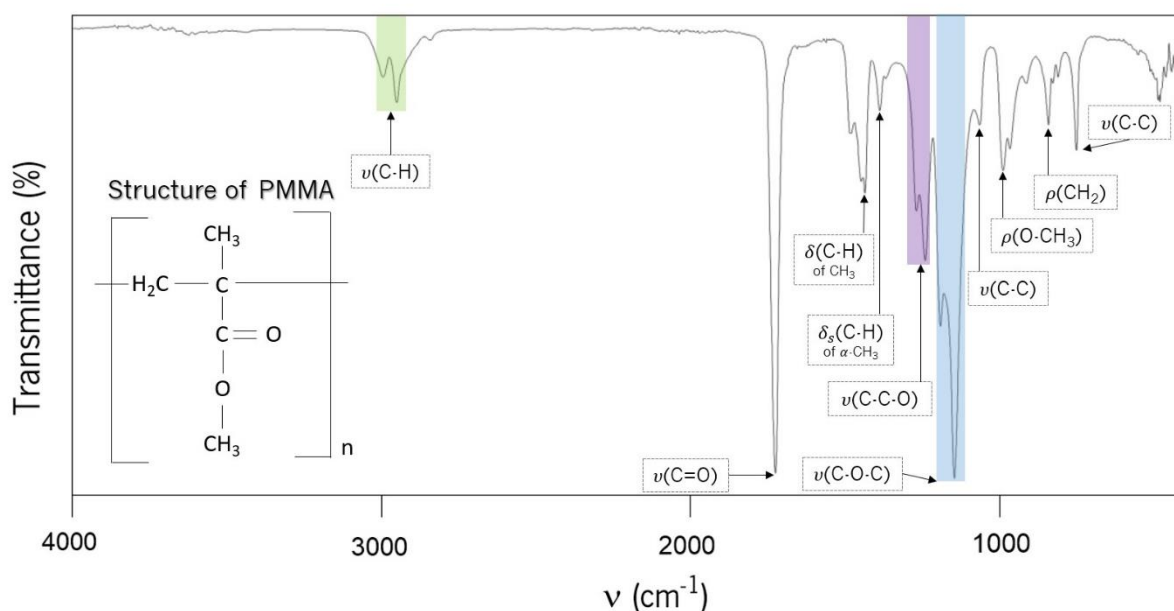


Figure 3-1 ATR-FTIR spectrum of the synthesized PMMA colloidal spheres.

Through a close analysis of the ATR-FTIR spectrum, the following vibrations of the PMMA groups can be assigned, which are in agreement with published spectra of PMMA. The bands at 2994 cm^{-1} and 2950 cm^{-1} can be assigned to stretching vibrational modes of CH_3 and CH_2 groups^{90,91}. The band at 1725 cm^{-1} corresponds to the $\text{C}=\text{O}$ stretching mode of the acrylate carbonyl group. The band at 1435 cm^{-1} is assigned to bending vibrations of C-H bonds of the CH_3 , and at 1387 cm^{-1} is the symmetric bending vibration of C-H of $\alpha\text{-CH}_3$ ⁹⁰⁻⁹². The bands located at 1268 cm^{-1} and 1240 cm^{-1} can be attributed to C-C-O stretching modes and at 1191 cm^{-1} and 1146 cm^{-1} are the C-O-C stretching vibrations^{82,90,92}. At 988 cm^{-1} the band can be assigned to O-CH_3 rocking vibration, coupled with the C-O-C stretching vibration, and at

841 cm^{-1} the rocking vibration of CH_2 group^{82,92}. The bands at 1064 cm^{-1} and 750 cm^{-1} can be assigned to vibrations of the polymer chains^{90,92}.

3.1.2. SEM and DLS analysis

The structural appearance of the PMMA spheres was determined by SEM methodology. SEM surface morphology of the PMMA spheres is shown in Figure 3-2 with 50000 \times and 100000 \times magnifications, where the particles show uniform morphology with spherical shape. Combining these micrographs (where 50 spheres were considered) with the ImageJ software, it was also possible to determine that the average diameter (D_{avg}) of the spheres was estimated around 231.1 ± 8.2 nm.

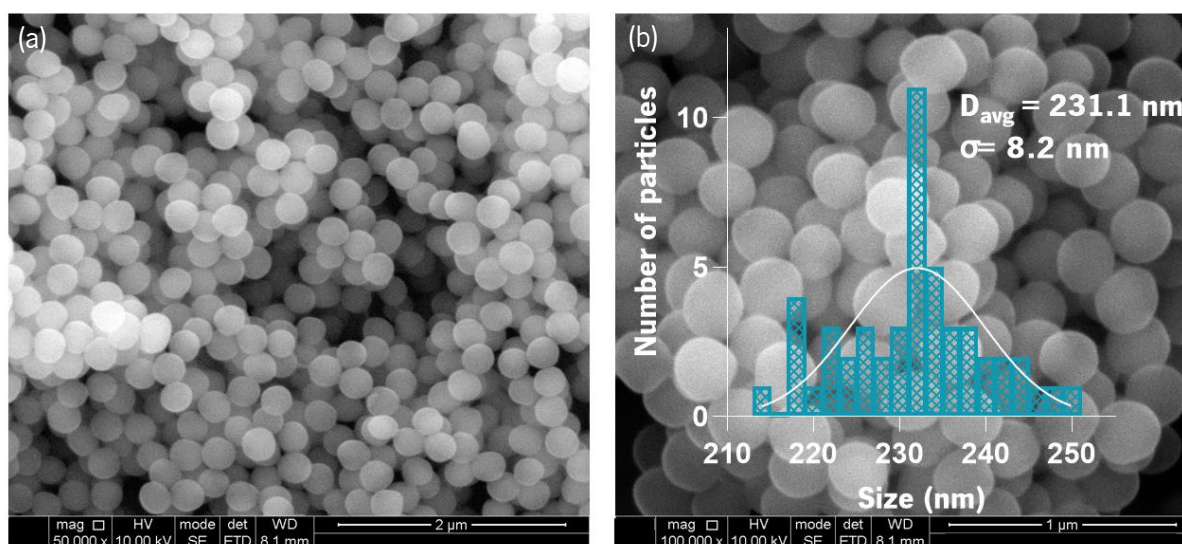


Figure 3-2 SEM micrographs of the PMMA colloidal spheres: **(a)** 50000 \times and **(b)** 100000 \times . The inset presents the size distribution histogram of the PMMA spheres of the sample.

The PMMA spheres were also analysed by DLS, which reported a D_{avg} of 365.6 ± 6.3 nm. By this analysis, it was found that D_{avg} of PMMA spheres measured by DLS is greater than the one given by SEM. This difference was expected because DLS measures the hydrodynamic size, which includes an electrical double layer around the particle. Also, the apparent hydrodynamic diameter is larger in low concentration ionic medium, which is the case of the current measurements⁹³. Moreover, it has been described that PMMA spheres contract under the action of an electron beam and that the rate of contraction depends on the current density⁸³. As the current density also depends on the scanning area,

by increasing the magnification, a quick contraction of the particles is observed. It has been proposed by other authors⁷⁵ that the local heating of the particles by the electron probe results in the release of the contents of the nanopores, so that they collapse and the spheres contract.

Having a highly monodisperse and stable colloidal suspension is considered as an essential prerequisite for the opal fabrication by means of particle self-assembly. The DLS analysis also demonstrated that the average PDI of the synthesized PMMA spheres was low, *i.e.*, 0.120 ± 0.045 . The PDI is dimensionless and is calculated from a two-parameter fit to the correlation data (the cumulants analysis), so that values bigger than 0.7 suggest a very broad particle size distribution in the sample^{94,95}. The analysis of the surface charge by zeta potential measurements using the DLS system showed a negative zeta potential of about -36.4 ± 1.0 mV, which means that the spheres are negatively charged. Since this value is outside the range of -30 mV to +30 mV, it indicates that the dispersion is stable due to electrostatic repulsion between particles of the same charge^{96,97}.

The results from SEM and DLS analyses led to conclude that the synthesis was successful in obtaining spherical, uniform, monodisperse PMMA colloids with a size on the nanoscale, making them the perfect building blocks for the opal fabrication.

3.2. Characterization of the PMMA opal film

The crystalline structure of the deposited film was studied using SEM analysis. Figure 3-3 shows SEM micrographs (both cross-section (a) and top view (b,c)) of the PMMA spheres forming an opal or colloidal crystal. The self-organization properties and some degree of intrinsic disorder that is inevitable in the self-assemble process of the colloidal spheres can be observed (Figure 3-3(b)). At higher magnification, the SEM image (Figure 3-3(c)) illustrates an excellent 3D order of the opal. Some regions with continuous periodic array can be seen in more detail, showing hexagons inside the densely packed crystal of spheres, which confirms the formation of a close-packed face-centered cubic (fcc) structure at the (111) crystal plane parallel to the substrate. In this sense, the uniformity and organization of the periodic structure of the opal on the glass substrate became evident, presenting a high degree of ordering with large domains⁹².

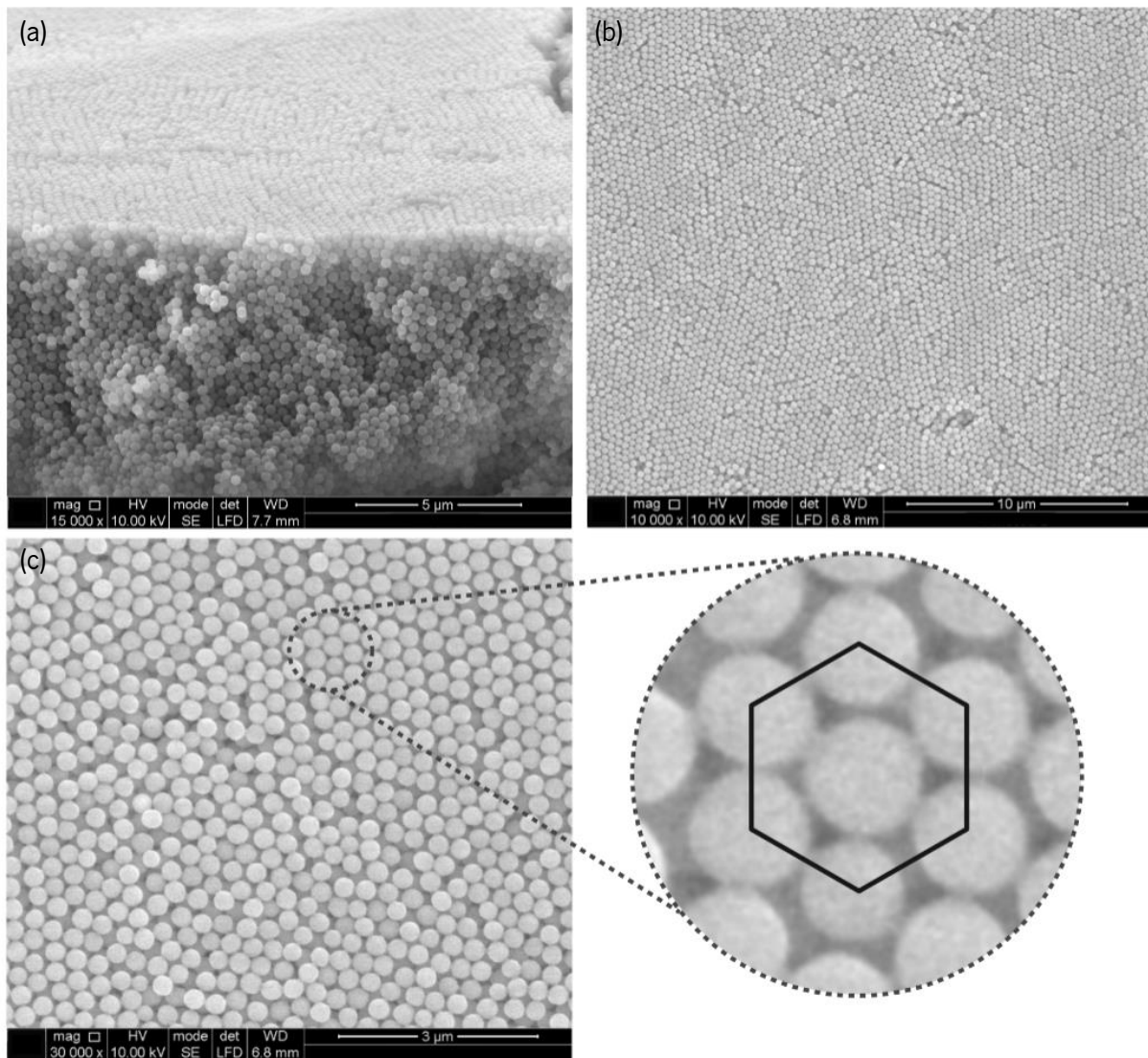


Figure 3-3 SEM images of PMMA opals, showing self-assembled spheres: **(a)** cross-sectional 15000×, **(b)** top view 10000× and **(c)** top view 30000× with an inset illustrating the close-packing fcc (black hexagon in the image).

The optical properties of the 3D PhC were then characterized by analysing the reflectance intensity. The reflectance spectrum was collected using the optical fiber probe at an angle of 45°, showing a reflectance peak at around 520 nm (Figure 3-4).

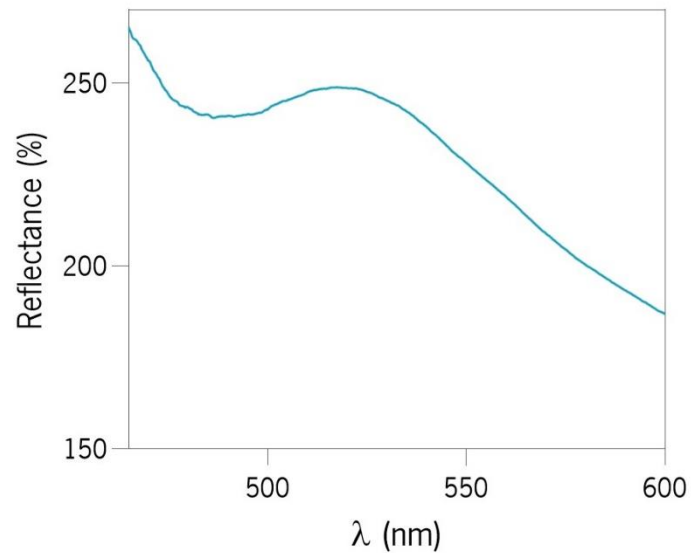


Figure 3-4 Reflectance spectrum of the opal structure (incident light at an angle of 45°).

3.3. Characterization of the hydrogel-based MIPP

The hydrogel-based MIPP was characterized using SEM analysis. It can be observed in Figure 3-5 (cross-section (a) and top view (b)) that the highly periodic ordered structure of the 3D PMMA array was completely preserved in the hydrogel. It is possible to observe the spheres entangled within the polymer network while keeping the periodic arrangement. The complete imprinting process of the opal structure onto the hydrogel was successfully attained as it was a crucial step with great influence on the responsive behaviour of the sensor.

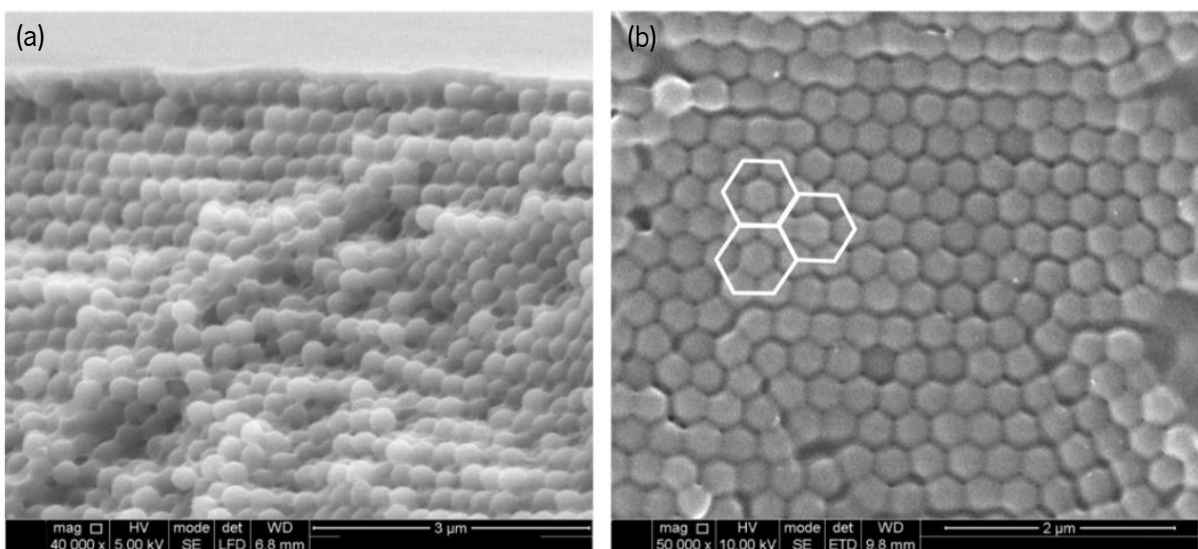


Figure 3-5 SEM images of the hydrogel-based MIPP, showing the imprinting of the PMMA opal structure: **(a)** cross-sectional $40000\times$ and **(b)** top view $50000\times$ with white hexagons illustrating the close-packing that was kept in the hydrogel.

Similarly to the optical characterization done to the PMMA opal film, also the hydrogel-based MIPP was characterized in terms of optical properties. The reflectance spectrum (incident light at 45°) was obtained (Figure 3-6). In comparison to the opal film on glass, a shift in the reflectance peak was observed in the hydrogel-based MIPP and the peak appeared around 563 nm. Also, the intensity of the peak decreased in comparison to the opal on glass. These changes are related to the interstitial filling of the opal with the hydrogel due to a decrease in the refractive index contrast, accompanied by positive change in the average refractive index, resulting in a decrease in the reflectance intensity and a red shift of the peak^{32,98}.

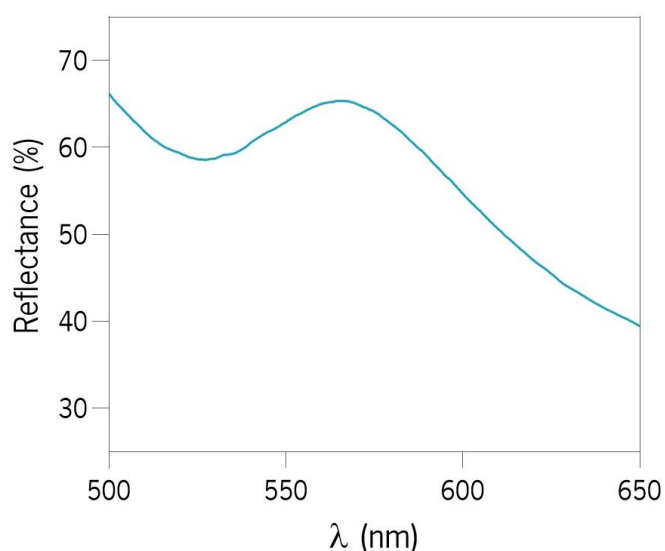


Figure 3-6 Reflectance spectrum of the hydrogel-based MIPP (incident light at an angle of 45°).

This construction makes the sensor developed in this work to rely on the responsiveness of the hydrogel to external stimuli and can be used as a colorimetric sensor. The changes that occur in the imprinted hydrogel upon detection of the target analyte are tracked by an optical signal, making this photonic hydrogel sensor expected to provide a highly sensitive and cost-effective method.

3.4. Optical response of the hydrogel-based MIPP towards the CD9 protein

The sensing ability of the sensor towards the CD9 protein was evaluated in order to determine its quantitative properties. In this sense, the optical response of the sensor at successive increasing concentrations of CD9 protein (25 pg mL^{-1} – 5859 pg mL^{-1}) was evaluated by measuring the reflectance

peak. The calibration curves were traced for the hydrogel-based MIPP in two matrices: PBS buffer and human serum. The same procedures were followed on NIPP as control material (Figure 3-7). The analysis of the obtained calibration curves prompt to conclude that consecutive increases of the CD9 protein concentration, both in PBS buffer as well as in serum, changed the optical properties of the MIPP sensor, namely a decrease in the peak intensity. During the molecular recognition, the binding of the target molecule with a different refractive index from the host matrix causes variations in the average refractive index, originating changes in the reflectance signal of the sensor^{99,100}. Although it was not observed a shift of the Bragg's diffraction peak, a significance decrease of the intensity of the MIPP's reflectance was evident in a concentration dependent way, as can be seen in Figure 3-7(a,c). Generally, a more significant effect on the structural colours arises from changing the diffracting plane spacing rather than the refractive index changes¹⁰⁰. Thus, the observed decrease may be attributed to an alteration of the refractive index in the presence of the CD9 protein.

In terms of analytical features, a linear relationship between the relative reflectance intensity (I/I_0) of the MIPP and the logarithm value of the CD9 protein concentration ($\log [CD9]$) was obtained in the range of 25 pg mL^{-1} to 2344 pg mL^{-1} for both matrices. The calibration curve in PBS buffer is shown in Figure 3-7(e) and the linear fitting equation is presented as the Equation 3-1.

$$I/I_0 = -(0.248 \pm 0.021) \log[CD9] (\text{pg mL}^{-1}) + (1.254 \pm 0.052); R^2 = 0.996$$

Equation 3-1

A LOD of 11 pg mL^{-1} was determined in PBS buffer. For the NIPP control, as the CD9 protein concentration gradually increases, the intensity of the reflectance maximum peak changes randomly, as shown in Figure 3-7(b,d), indicating that the NIPP has no response to the CD9 protein. This is because the NIPP does not have selective recognition sites to the CD9 molecule, and the observed changes are caused by nonspecific adsorption. These results suggest that the sensor is responsive to CD9 protein due to the nanocavities that have shape, size and functional groups that match the CD9 protein in the 3D network of the MIPP after the CD9 molecules imprinted on the PhC hydrogel were eluted. In the presence of the CD9 molecules, the protein can specifically bind to these nanocavities.

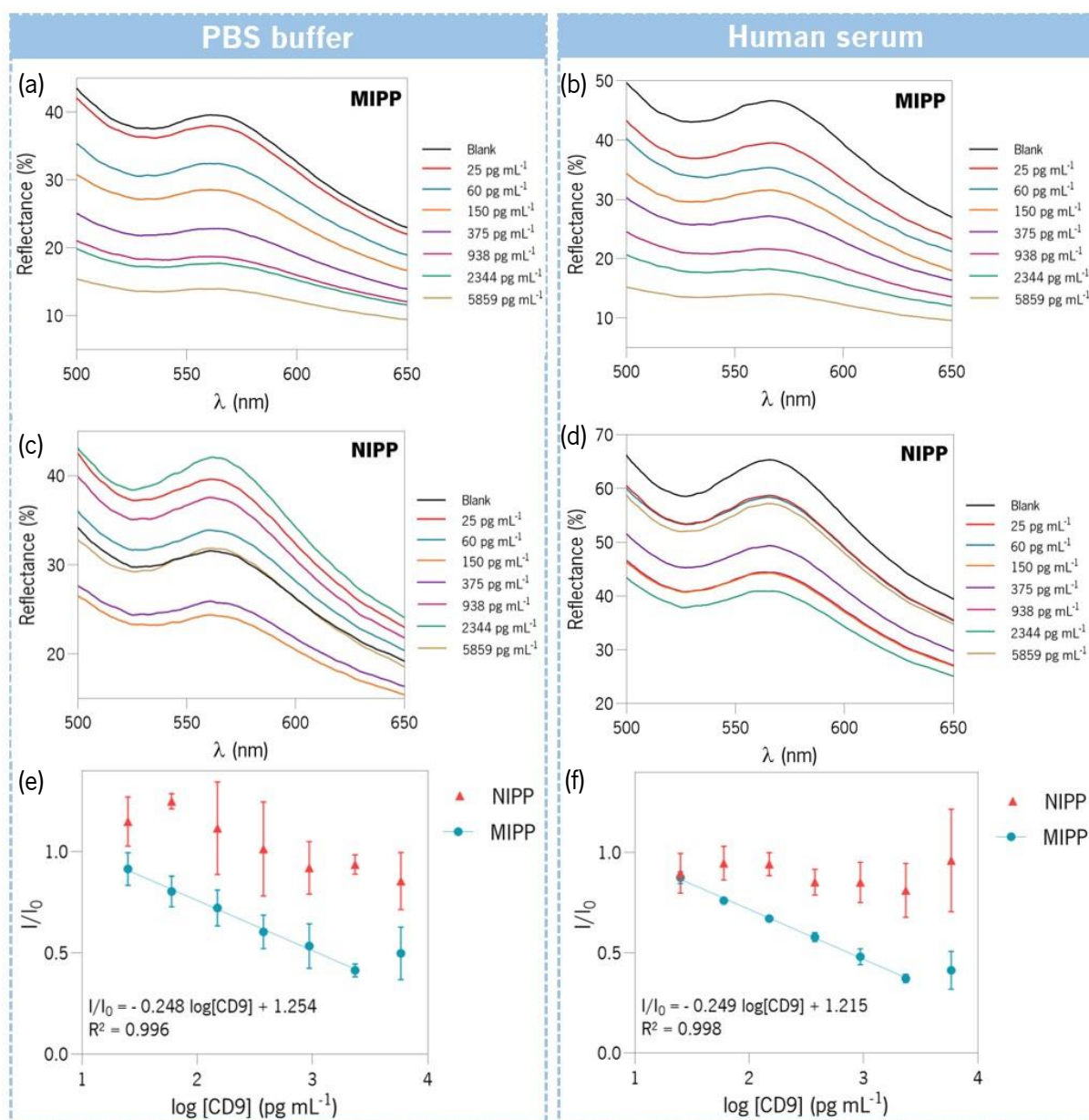


Figure 3-7 Optical response of the hydrogel-based MIPP (**a, b**) and the NIPP control (**c, d**) to CD9 protein in PBS buffer (0.01 mol L^{-1} , $\text{pH} = 7.4$) (**a, c**) and in human serum (1000-fold diluted) (**b, d**), expressed by reflectance intensity, and the corresponding calibration curves in PBS buffer (**e**) and in serum (**f**) ($n=3$).

Similar experiments were performed in human serum (diluted 1000-fold) to test the response ability of the sensor towards the CD9 protein in a more complex matrix. As observed in PBS buffer, the MIPP material evidenced a decreasing trend of the reflectance intensity upon binding of the CD9 protein, while the NIPP material had a random response, as can be seen in Figure 3-7 (b,d). In this matrix, the linear fitting equation is presented as Equation 3-2.

$$I/I_0 = -(0.249 \pm 0.014) \log[\text{CD9}] (\text{pg mL}^{-1}) + (1.215 \pm 0.035); R^2 = 0.998$$

Equation 3-2

The LOD in serum was determined to be 19 pg mL^{-1} , higher than the LOD obtained in PBS buffer. Nonetheless, the slopes of the calibration curves in both matrices were similar, suggesting that the sensitivity of the sensor was not reduced in serum. These results are very promising considering that the sensor could be used in more complex biological samples.

The accuracy of the sensor response was evaluated by spiking human serum with two known concentrations of CD9 protein (90 pg mL^{-1} and 690 pg mL^{-1}). The average errors obtained were $17 \pm 7 \%$ for 90 pg mL^{-1} , and $23 \pm 3 \%$ for 690 pg mL^{-1} ($n=3$). Thus, the determined average values were consistent with the spiked theoretical levels. These good results indicate that the MIPP sensor enables accurate analysis of the CD9 protein within the tested concentration range.

3.5. Optical response of the hydrogel-based MIPP towards EVs

The sensing ability of the hydrogel-based MIPP towards EVs was evaluated in order to determine if EVs could be captured through the recognition cavities designed for the CD9 protein. For this purpose, the reflectance of the MIPP sensor was measured after incubation with three different concentrations of EVs isolated from astrocytes and diluted in human serum, using NIPP as control (Figure 3-8).

The obtained data suggests that the sensing material is able to recognize and capture EVs with an outcome change in the optical properties, *i.e.*, by showing a decrease in the reflectance intensity. The results showed that a concentration as low as $6.85 \times 10^1 \text{ } \mu\text{L}^{-1}$ elicited a sensor response. However, a more pronounced effect was observed for increasing concentrations up to $10^5 \text{ } \mu\text{L}^{-1}$. The ANOVA analysis revealed that there was a statistically significant difference, $F(3, 8) = 25.83$, $p = 0.0002$, between the hydrogel-based MIPP responses to various concentrations of EVs. Also, there was a significant linear trend, $F(1, 8) = 77.07$, $p < 0.0001$, indicating that as the concentration of EVs increased, sensor responded proportionately by an decrease in the reflectance intensity. The NIPP used as control material showed a random change, indicating that the recognition of EVs by the MIPP was due to the nanocavities that match the CD9 protein in the network. Like the recognition of CD9 protein, the observed decrease in the intensity of the reflectance peak caused by the presence of EVs in the MIPP may result from changes in the average refractive index.

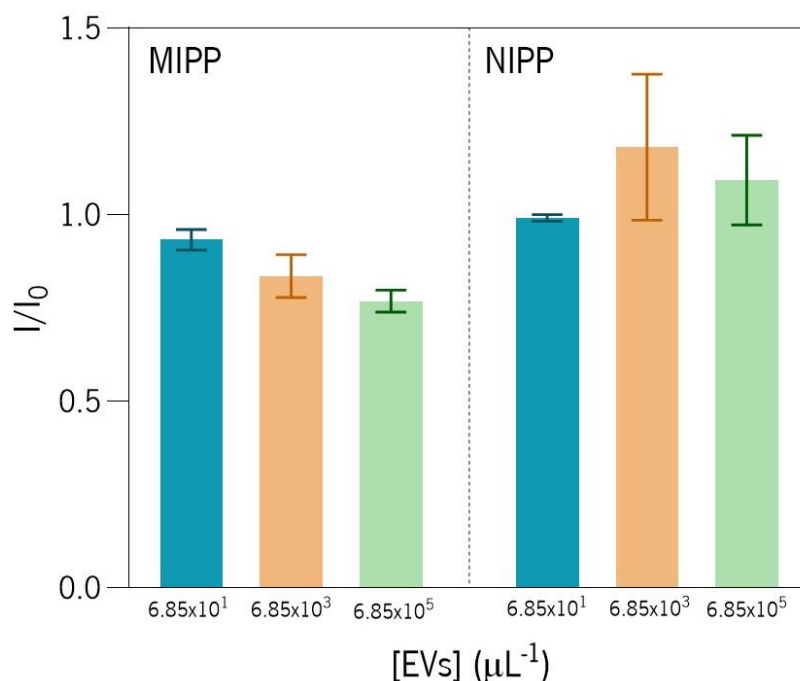


Figure 3-8 Response of the sensor MIPP and respective NIPP control to three different EVs unitary concentrations ($6.85 \times 10^1 \mu\text{L}^{-1}$, $6.85 \times 10^3 \mu\text{L}^{-1}$ and $6.85 \times 10^5 \mu\text{L}^{-1}$) prepared in human serum (diluted 1000-fold) ($n=3$).

3.6. Selectivity studies by testing CD81 and GLAST-1 proteins

In order to study the selectivity of the MIPP sensor towards CD9 protein, two other proteins considered surface markers of EVs were tested. The chosen proteins, CD81 and GLAST-1, were prepared in human serum at low and high concentrations, but in the range of the linear response for CD9. The reflectance peak did not decrease after incubation with either protein at any of the tested concentrations. Thus, no following statistical analysis was considered. The control NIPP was also tested and showed random response, as expected (Figure 3-9). These results, also comparing sensor's response to CD9 protein at similar concentrations that originated a significant decrease in the reflectance intensity, suggest that the hydrogel-based MIPP has good selectivity for CD9 protein. The nonspecific adsorption of CD81 and GLAST-1 may account for the very small random changes observed in the MIPP, like in the NIPP. Thus, the obtained results suggest that the imprinted nanocavities for CD9 protein, which is partially on the surface of EVs, are accounted for the recognition of EVs by the sensing material.

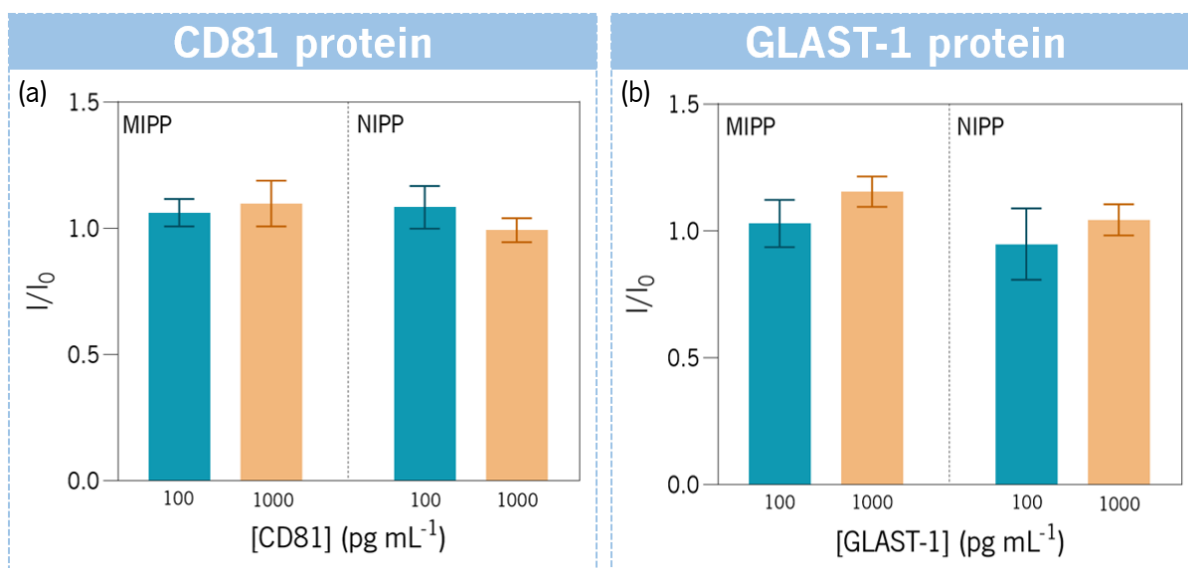


Figure 3-9 Response of the sensor MIPP and respective NIPP control to two different CD81 **(a)** and GLAST-1 **(b)** protein concentrations (100 pg mL^{-1} and 1000 pg mL^{-1}) prepared in human serum (diluted 1000-fold) ($n=3$).

Chapter 4. Conclusions and future work

EVs have a huge potential in clinical applications but, as highlighted, there are still many unknowns in the field. More precisely, there is still a lack of accurate methods for the isolation of EVs and characterization of different subpopulations, to which an origin and function can be attributed. In this sense, MIPs coupled to sensitive optical transduction can be the key to overcome these limitations and allow an effective isolation of EVs, making possible a more precise understanding of their functions and the development of novel therapeutic strategies.

In this work, PhC and molecularly imprinting technologies were combined to prepare a highly ordered 3D hydrogel that displays selective and sensitive CD9 protein recognition properties. The synthesized hydrogel-based MIPP directly couple a readable optical signal, without the need for labelling, upon protein recognition events on the imprinted sites. By combining the selectivity of the MIP materials and the organized structure of a PhC with optical properties, the MIPP sensor exhibited high sensitivity for the CD9 protein, demonstrating a linear response between 25 pg mL^{-1} and 2344 pg mL^{-1} , while displaying a low detection limit (19 pg mL^{-1} in human serum). Moreover, as the final aim is to deploy novel sensing materials able to improve the selective isolation and recovery of circulating EVs, the recognition ability towards EVs derived from astrocyte cells was studied. The results showed that the sensor responded to a concentration as low as $6.85 \times 10^1 \mu\text{L}^{-1}$ but recognized EVs in a wide range, *i.e.*, up to $6.85 \times 10^5 \mu\text{L}^{-1}$ in serum samples. Subsequent assays suggested that the sensor was selective for CD9, as it did not respond to other similar proteins, namely CD81 and GLAST-1. These results are relevant considering that the EVs should be captured by a specific surface marker, and thus this sensing material can be useful for analysing subpopulations of EVs.

Due to the low-cost materials herein developed, future studies could offer similar mimetic hydrogels for other target proteins present on the surface of EVs and even investigate the introduction of functional moieties in the polymer to improve the interaction with EVs and their capture from body fluids. Other interesting application should be the integration of the developed sensor in miniaturized microfluidic tools. In conclusion, the presented technology has promising features to enable improved recovery and isolation of EVs in future sensing devices.

Bibliography

1. Torrano, V. *et al.* Vesicle-MaNiA: Extracellular vesicles in liquid biopsy and cancer. *Curr. Opin. Pharmacol.* **29**, 47–53 (2016).
2. Sunkara, V., Woo, H. K. & Cho, Y. K. Emerging techniques in the isolation and characterization of extracellular vesicles and their roles in cancer diagnostics and prognostics. *Analyst* **141**, 371–381 (2016).
3. Colombo, M., Raposo, G. & Théry, C. Biogenesis, secretion, and intercellular interactions of exosomes and other extracellular vesicles. *Annu. Rev. Cell Dev. Biol.* **30**, 255–289 (2014).
4. Bungulawa, E. J. *et al.* Recent advancements in the use of exosomes as drug delivery systems 06 Biological Sciences 0601 Biochemistry and Cell Biology. *J. Nanobiotechnology* **16**, 1–13 (2018).
5. Doyle, L. & Wang, M. Overview of Extracellular Vesicles, Their Origin, Composition, Purpose, and Methods for Exosome Isolation and Analysis. *Cells* **8**, 727 (2019).
6. Tkach, M. & Théry, C. Communication by Extracellular Vesicles: Where We Are and Where We Need to Go. *Cell* **164**, 1226–1232 (2016).
7. Yang, X. X., Sun, C., Wang, L. & Guo, X. L. New insight into isolation, identification techniques and medical applications of exosomes. *J. Control. Release* **308**, 119–129 (2019).
8. Li, S.-R. *et al.* Tissue-derived extracellular vesicles in cancers and non-cancer diseases: Present and future. *J. Extracell. Vesicles* **10**, e12175 (2021).
9. Couch, Y. *et al.* A brief history of nearly EV-erything – The rise and rise of extracellular vesicles. *J. Extracell. Vesicles* **10**, e12144 (2021).
10. Théry, C. *et al.* Minimal information for studies of extracellular vesicles 2018 (MISEV2018): a position statement of the International Society for Extracellular Vesicles and update of the MISEV2014 guidelines. **7**, (2018).
11. Zaborowski, M. P., Balaj, L., Breakefield, X. O. & Lai, C. P. Extracellular Vesicles: Composition, Biological Relevance, and Methods of Study. *Bioscience* **65**, 783–797 (2015).
12. Veziroglu, E. M. & Mias, G. I. Characterizing Extracellular Vesicles and Their Diverse RNA Contents. *Front. Genet.* **11**, 700 (2020).
13. Andreu, Z. & Yáñez-Mó, M. Tetraspanins in extracellular vesicle formation and function. *Front. Immunol.* **5**, 442 (2014).
14. Jankovičová, J., Sečová, P., Michalková, K. & Antalíková, J. Tetraspanins, More than Markers of Extracellular Vesicles in Reproduction. *Int. J. Mol. Sci.* **21**, 1–30 (2020).
15. Gurunathan, S., Kang, M., Jeyaraj, M., Qasim, M. & Kim, J. Function, and Multifarious Therapeutic Approaches of Exosomes. *Cells* **8**, 307 (2019).
16. Cardoso, A. R., Tavares, A. P. M. & Sales, M. G. F. In-situ generated molecularly imprinted material for chloramphenicol electrochemical sensing in waters down to the nanomolar level. *Sensors Actuators, B Chem.* **256**, 420–428 (2018).

17. Chen, Y. T. *et al.* Review of Integrated Optical Biosensors for Point-Of-Care Applications. *Biosensors* **10**, 1–22 (2020).
18. Turiel, E. & Esteban, A. M. *Molecularly imprinted polymers. Solid-Phase Extraction* (Elsevier Inc., 2019).
19. Chen, L., Wang, X., Lu, W., Wu, X. & Li, J. Molecular imprinting: Perspectives and applications. *Chem. Soc. Rev.* **45**, 2137–2211 (2016).
20. Włoch, M. & Datta, J. Synthesis and polymerisation techniques of molecularly imprinted polymers. *Compr. Anal. Chem.* **86**, 17–40 (2019).
21. Mori, K. *et al.* A Pretreatment-Free, Polymer-Based Platform Prepared by Molecular Imprinting and Post-Imprinting Modifications for Sensing Intact Exosomes. *Angew. Chemie - Int. Ed.* **58**, 1612–1615 (2019).
22. Takeuchi, T. *et al.* Antibody-Conjugated Signaling Nanocavities Fabricated by Dynamic Molding for Detecting Cancers Using Small Extracellular Vesicle Markers from Tears. *J. Am. Chem. Soc.* **142**, 6617–6624 (2020).
23. Chen, C. & Wang, J. Optical biosensors: An exhaustive and comprehensive review. *Analyst* **145**, 1605–1628 (2020).
24. Chen, W., Meng, Z., Xue, M. & Shea, K. J. Molecular imprinted photonic crystal for sensing of biomolecules. *Mol. Imprinting* **4**, 1–12 (2016).
25. Shao, J., Liu, G. & Zhou, L. *Biomimetic nanocoatings for structural coloration of textiles. Active Coatings for Smart Textiles* (Elsevier Ltd, 2016).
26. Mayonado, G., Mian, S. M., Robbiano, V. & Cacialli, F. Investigation Of The Bragg-Snell Law In Photonic Crystals. 60–63 (2015).
27. Xuan, Z. *et al.* Artificial Structural Colors and Applications. *Innov.* **2**, 100081 (2021).
28. Daqiqeh Rezaei, S. *et al.* Nanophotonic Structural Colors. *ACS Photonics* **8**, 18–33 (2020).
29. Gao, W., Owens, H. & Rigout, M. Structural colours from self-assembled silica nanoparticles for textile coloration silica nanoparticles for textile coloration. *Adv. Mater. their Appl. - Micro to nano scale* 307–323 (2018).
30. Sun, J., Bhushan, B. & Tong, J. Structural coloration in nature. *RSC Adv.* **3**, 14862–14889 (2013).
31. Chiappini, A., Pasquardini, L. & Bossi, A. M. Molecular imprinted polymers coupled to photonic structures in biosensors: The state of art. *Sensors (Switzerland)* **20**, 1–23 (2020).
32. Phillips, K. R. *et al.* A colloidoscope of colloid-based porous materials and their uses. *Chem. Soc. Rev.* **45**, 281–322 (2016).
33. Marie, H. & To. Elaboration of a new sensor based on molecularly imprinted polymers for the detection of molecules in physiological fluids. HAL Id: tel-00977390 <https://tel.archives-ouvertes.fr/tel-00977390> (Université de Technologie de Compiègne, 2013).

34. Yu, H.-D., Regulacio, M. D., Ye, E. & Han, M.-Y. Chemical routes to top-down nanofabrication. *Chem. Soc. Rev* **42**, 6006 (2013).
35. Zheng, H. & Ravaine, S. Bottom-up assembly and applications of photonic materials. *Crystals* **6**, (2016).
36. Biswas, A. *et al.* Advances in top-down and bottom-up surface nanofabrication: Techniques, applications & future prospects. *Adv. Colloid Interface Sci.* **170**, 2–27 (2012).
37. López, J. *An optical study of opal based photonic crystals.* (2005).
38. Bertholdo, R. *et al.* Fabrication and analysis of self-assembled photonic crystals structures. *SBMO/IEEE MTT-S Int. Microw. Optoelectron. Conf. Proc.* 50–53 (2007).
39. Waterhouse, G. I. N. & Waterland, M. R. Opal and inverse opal photonic crystals : Fabrication and characterization. **26**, 356–368 (2007).
40. Lu, Z. & Zhou, M. Fabrication of large scale two-dimensional colloidal crystal of polystyrene particles by an interfacial self-ordering process. *J. Colloid Interface Sci.* **361**, 429–435 (2011).
41. Eslamian, M. & Zabihi, F. Ultrasonic Substrate Vibration-Assisted Drop Casting (SVADC) for the Fabrication of Photovoltaic Solar Cell Arrays and Thin-Film Devices. *Nanoscale Res. Lett.* **10**, 1–5 (2015).
42. Chen, X., Hu, Y., Xie, Z. & Wang, H. Materials and Design of Photocatalytic Membranes. in *Current Trends and Future Developments on (Bio-) Membranes: Photocatalytic Membranes and Photocatalytic Membrane Reactors* 71–96 (Elsevier Inc., 2018).
43. Vogel, N., Goerres, S., Landfester, K. & Weiss, C. K. A Convenient Method to Produce Close- and Non-close-Packed Monolayers using Direct Assembly at the Air-Water Interface and Subsequent Plasma-Induced Size Reduction. *Macromol. Chem. Phys.* **212**, 1719–1734 (2011).
44. Chen, X. *et al.* Langmuir-blodgett patterning: A bottom-up way to build mesostructures over large areas. *Acc. Chem. Res.* **40**, 393–401 (2007).
45. Lu, Z. *et al.* Direct assembly of hydrophobic nanoparticles to multifunctional structures. *Nano Lett.* **11**, 3404–3412 (2011).
46. Kaliyaraj Selva Kumar, A., Zhang, Y., Li, D. & Compton, R. G. A mini-review: How reliable is the drop casting technique? *Electrochemistry Communications* vol. 121 106867 (2020).
47. Zheng, H. & Ravaine, S. Bottom-Up Assembly and Applications of Photonic Materials. (2016) doi:10.3390/cryst6050054.
48. Kajal, P., Ghosh, K. & Powar, S. Manufacturing Techniques of Perovskite Solar Cells Manufacturing Techniques of Perovskite Solar Cells. (2018).
49. Meijer, J. M. *et al.* Self-assembly of colloidal cubes via vertical deposition. *Langmuir* **28**, 7631–7638 (2012).
50. Sahoo, S. K., Manoharan, B. & Sivakumar, N. Introduction: Why perovskite and perovskite solar cells? in *Perovskite Photovoltaics: Basic to Advanced Concepts and Implementation* 1–24 (Elsevier, 2018).

51. Snoswell, D. R. E. *et al.* Shear ordering in polymer photonic crystals. *Phys. Rev. E - Stat. Nonlinear, Soft Matter Phys.* **81**, (2010).
52. Amos, R. M., Rarity, J. G., Tapster, P. R., Shepherd, T. J. & Kitson, S. C. Fabrication of large-area face-centered-cubic hard-sphere colloidal crystals by shear alignment. *Phys. Rev. E - Stat. Physics, Plasmas, Fluids, Relat. Interdiscip. Top.* **61**, 2929–2935 (2000).
53. Juarez-Martinez, G. *et al.* Macromolecular Crystallization Using Nano-volumes. in *Encyclopedia of Nanotechnology* 1235–1248 (Springer Netherlands, 2012). doi:10.1007/978-90-481-9751-4_126.
54. Diao, J. J., Hutchison, J. B., Luo, G. & Reeves, M. E. Theoretical analysis of vertical colloidal deposition. *J. Chem. Phys.* **122**, (2005).
55. Fan, W., Chen, M., Yang, S. & Wu, L. Centrifugation-assisted Assembly of Colloidal Silica into Crack-Free and Transferrable Films with Tunable Crystalline Structures. *Sci. Rep.* **5**, 12100 (2015).
56. Oh, J. R., Moon, J. H., Yoon, S., Park, C. R. & Do, Y. R. Fabrication of wafer-scale polystyrene photonic crystal multilayers via the layer-by-layer scooping transfer technique. **21**, 41–58 (2011).
57. Hu, X., An, Q., Li, G., Tao, S. & Liu, J. Imprinted Photonic Polymers for Chiral Recognition. *Angew. Chemie Int. Ed.* **45**, 8145–8148 (2006).
58. Hu, X., Li, G., Huang, J., Zhang, D. & Qiu, Y. Construction of Self-Reporting Specific Chemical Sensors with High Sensitivity. *Adv. Mater.* **19**, 4327–4332 (2007).
59. Hu, X. *et al.* Ultrasensitive Specific Stimulant Assay Based on Molecularly Imprinted Photonic Hydrogels. *Adv. Funct. Mater.* **18**, 575–583 (2008).
60. Wu, Z. *et al.* Direct and label-free detection of cholic acid based on molecularly imprinted photonic hydrogels. *J. Mater. Chem.* **18**, 5452–5458 (2008).
61. Wu, Z., Tao, C., Lin, C., Shen, D. & Li, G. Label-Free Colorimetric Detection of Trace Atrazine in Aqueous Solution by Using Molecularly Imprinted Photonic Polymers. *Chem. - A Eur. J.* **14**, 11358–11368 (2008).
62. Griffete, N. *et al.* Introduction of a planar defect in a molecularly imprinted photonic crystal sensor for the detection of bisphenol A. *J. Colloid Interface Sci.* **364**, 18–23 (2011).
63. Li, J. *et al.* Label-free colorimetric detection of trace cholesterol based on molecularly imprinted photonic hydrogels. *J. Mater. Chem.* **21**, 19267–19274 (2011).
64. Chen, Z., Zhao, W., Luo, A., Palomino, P. & Enciso, E. Imprinted photonic crystals for levodropropizine sensing. in *2012 Symposium on Photonics and Optoelectronics, SOPO 2012* (2012).
65. Griffete, N. *et al.* Inverse opals of molecularly imprinted hydrogels for the detection of bisphenol A and pH sensing. *Langmuir* **28**, 1005–1012 (2012).
66. Guo, C. *et al.* Detection of bisphenol A using an opal photonic crystal sensor. *Sensors Actuators, B Chem.* **166–167**, 17–23 (2012).

67. Liu, F. *et al.* Detection of organophosphorus compounds using a molecularly imprinted photonic crystal. *Biosens. Bioelectron.* **32**, 273–277 (2012).
68. Peng, H. *et al.* Molecularly imprinted photonic hydrogels as colorimetric sensors for rapid and label-free detection of vanillin. *J. Agric. Food Chem.* **60**, 1921–1928 (2012).
69. Wang, L. Q., Lin, F. Y. & Yu, L. P. A molecularly imprinted photonic polymer sensor with high selectivity for tetracyclines analysis in food. *Analyst* **137**, 3502–3509 (2012).
70. Xu, D. *et al.* Rational design of molecularly imprinted photonic films assisted by chemometrics. *J. Mater. Chem.* **22**, 16572–16581 (2012).
71. Zhou, C. *et al.* Molecularly imprinted photonic polymer as an optical sensor to detect chloramphenicol. *Analyst* **137**, 4469–4474 (2012).
72. Meng, L., Meng, P., Tang, B., Zhang, Q. & Wang, Y. Molecularly imprinted photonic hydrogels for fast screening of atropine in biological samples with high sensitivity. *Forensic Sci. Int.* **231**, 6–12 (2013).
73. Meng, L., Meng, P., Zhang, Q. & Wang, Y. Fast screening of ketamine in biological samples based on molecularly imprinted photonic hydrogels. *Anal. Chim. Acta* **771**, 86–94 (2013).
74. Wang, X., Mub, Z., Liu, R., Pu, Y. & Yin, L. Molecular imprinted photonic crystal hydrogels for the rapid and label-free detection of imidacloprid. *Food Chem.* **141**, 3947–3953 (2013).
75. Xue, F. *et al.* A covalently imprinted photonic crystal for glucose sensing. *J. Nanomater.* **2013**, (2013).
76. Zhang, Y. X., Zhao, P. Y. & Yu, L. P. Highly-sensitive and selective colorimetric sensor for amino acids chiral recognition based on molecularly imprinted photonic polymers. *Sensors Actuators, B Chem.* **181**, 850–857 (2013).
77. Zhang, Y. *et al.* Molecularly imprinted photonic crystals for the direct label-free distinguishing of l-proline and d-proline. *Phys. Chem. Chem. Phys.* **15**, 17250–17256 (2013).
78. Yang, Z., Shi, D., Chen, M. & Liu, S. Free-standing molecularly imprinted photonic hydrogels based on β -cyclodextrin for the visual detection of l-tryptophan. *Anal. Methods* **7**, 8352–8359 (2015).
79. Zhang, Y., Huang, S., Qian, C., Wu, Q. & He, J. Preparation of cinchonine molecularly imprinted photonic crystal film and its specific recognition and optical responsive properties. *J. Appl. Polym. Sci.* **133**, 43191 (2016).
80. Kadhem, A. J., Xiang, S., Nagel, S., Lin, C. H. & de Cortalezzi, M. F. Photonic molecularly imprinted polymer film for the detection of testosterone in aqueous samples. *Polymers (Basel)*. **10**, 349 (2018).
81. Wang, Y. *et al.* Fast screening of antibiotics in milk using a molecularly imprinted two-dimensional photonic crystal hydrogel sensor. *Anal. Chim. Acta* **1070**, 97–103 (2019).
82. Matamoros-Ambrocio, M., Sánchez-Mora, E., Gómez-Barojas, E. & Luna-López, J. A. Synthesis and Study of the Optical Properties of PMMA Microspheres and Opals. *Polym. 2021, Vol. 13, Page 2171* **13**, 2171 (2021).

83. Shabanova, O. V., Korshunov, M. A., Nemtsev, I. V. & Shabanov, A. V. Features of self-assembly of opal-like structures based on poly(methyl methacrylate) submicron dispersions. *Nanotechnologies Russ.* **11**, 633–639 (2016).
84. Pham, Q. Fabrication of Copper Inverse Opals for Microscale Liquid Transport in Polycrystalline Porous Media. (University of California, 2018).
85. International Organization for Standardization (ISO). Capability of Detection; Report No. ISO 11843-2. (2000).
86. McNaught, A. D. & Wilkinson, A. *IUPAC Compendium of Chemical Terminology*. (Blackwell Scientific Publications, 1997).
87. Inczedy, J., Lengyel, T., Ure, A. M., Gelencsér, A. & Hulanicki, A. *IUPAC Analytical Chemistry Division, Compendium of Analytical Nomenclature*. (Blackwell Scientific Publications, 1998).
88. Buck, R. P. & Lindner, E. Recommendations for nomenclature of ion-selective electrodes (IUPAC recommendations 1994). *Pure Appl. Chem.* **66**, 2527–2536 (1994).
89. Zhao, S. *et al.* Astrocyte-derived extracellular vesicles: A double-edged sword in central nervous system disorders. *Neurosci. Biobehav. Rev.* **125**, 148–159 (2021).
90. Bassan, P. *et al.* Resonant Mie scattering in infrared spectroscopy of biological materials – understanding the ‘dispersion artefact’. *Analyst* **134**, 1586–1593 (2009).
91. Mendes, A. N. *et al.* Encapsulation of Piper cabralanum (Piperaceae) nonpolar extract in poly(methyl methacrylate) by miniemulsion and evaluation of increase in the effectiveness of antileukemic activity in K562 cells. *Int. J. Nanomedicine* **12**, 8363 (2017).
92. Dazzi, A., Deniset-Besseau, A. & Lasch, P. Minimising contributions from scattering in infrared spectra by means of an integrating sphere. *Analyst* **138**, 4191–4201 (2013).
93. Schumacher, G. A. & Van De Ven, T. G. M. Brownian Motion of Charged Colloidal Particles surrounded by Electric Double Layers. *Furuday Discuss. Chem. SOC* **83**, 75–85 (1987).
94. Worldwide, M. I. Dynamic Light Scattering, Common Terms Defined. 1–6 (2011).
95. Danaei, M. *et al.* Impact of Particle Size and Polydispersity Index on the Clinical Applications of Lipidic Nanocarrier Systems. *Pharmaceutics* **10**, (2018).
96. Melo, L. O., Ponzio, E. A., Carmona-Ribeiro, A. M. & Torres, R. M. Poly(aniline)/poly(methylmethacrylate) films obtained from waterborne latex nanoparticles. *E-Polymers* **8**, 149 (2008).
97. Joseph, E. & Singhvi, G. Multifunctional nanocrystals for cancer therapy: a potential nanocarrier. *Nanomater. Drug Deliv. Ther.* 91–116 (2019).
98. Goerlitzer, E. S. A., Klupp Taylor, R. N. & Vogel, N. Bioinspired Photonic Pigments from Colloidal Self-Assembly. *Adv. Mater.* **30**, 1706654 (2018).
99. Burgess, I. B., Lončar, M. & Aizenberg, J. Structural colour in colourimetric sensors and indicators. *J. Mater. Chem. C* **1**, 6075–6086 (2013).

100. Zhao, Y., Xie, Z., Gu, H., Zhu, C. & Gu, Z. Bio-inspired variable structural color materials. *Chem. Soc. Rev.* **41**, 3297–3317 (2012).